

AD-A213 454

2

WAVE AND FRACTURE PHENOMENA  
IN IMPACTED CERAMICS

DTIC  
ELECTE  
OCT 11 1989  
S B D

S. Winkler (IWM, Principal Investigator)  
H. Senf and H. Rothenhäusler (EMI-AFB)

IWM-Bericht V 23/89  
December 1987 - May 1989

Vervielfältigung und Weiterverbreitung  
sind nur mit Zustimmung der FhG gestattet

DISTRIBUTION STATEMENT A  
Approved for public release;  
Distribution Unlimited

89 10 10215

DISTRIBUTION STATEMENT A  
Approved for public release;  
Distribution Unlimited

Prepared for European Research Office of the U.S. Army, London  
Contract Number DAJA45-88-C-0011  
IWM-Project 301 256  
Final Report

IWM  
Wöhlerstrasse 11, D-7800 Freiburg, West Germany

Fraunhofer-Institut für Kurzzeitdynamik (EMI-AFB)  
Ernst-Mach-Institut, Abteilung für Ballistik  
Hauptstrasse 18, D-7858 Weil am Rhein, West Germany

UNCLAS

SECURITY CLASSIFICATION OF THIS PAGE

REPORT DOCUMENTATION PAGE				Form Approved OMB No 0704 0188 Exp Date Jun 30 1986	
1a REPORT SECURITY CLASSIFICATION UNCLAS		1b RESTRICTIVE MARKINGS			
2a SECURITY CLASSIFICATION AUTHORITY		3 DISTRIBUTION/AVAILABILITY STATEMENT APPROVED FOR PUBLIC RELEASE; DISTRIBUTION UNLIMITED			
2b DECLASSIFICATION/DOWNGRADING SCHEDULE					
4 PERFORMING ORGANIZATION REPORT NUMBER(S) V 23/89		5 MONITORING ORGANIZATION REPORT NUMBER(S) R&D 5823-MS-01			
6a NAME OF PERFORMING ORGANIZATION FRÄUNHOFER INSTITUT FÜR WERKSTOFFMECHANIK		6b OFFICE SYMBOL (if applicable)	7a NAME OF MONITORING ORGANIZATION ERO USARDSG-UK		
6c ADDRESS (City, State, and ZIP Code) WOHLERSTRASSE 11 D-7800 FREIBURG FRG		7b ADDRESS (City, State, and ZIP Code) BOX 65 FPO NEW YORK 09150-1500			
8a NAME OF FUNDING/SPONSORING ORGANIZATION ERO USARDSG-UK		8b OFFICE SYMBOL (if applicable)	9 PROCUREMENT INSTRUMENT IDENTIFICATION NUMBER DAJA45-88-C-0011		
8c ADDRESS (City, State, and ZIP Code) BOX 65 FPO NEW YORK 09150-1500		10 SOURCE OF FUNDING NUMBERS			
		PROGRAM ELEMENT NO 61102A	PROJECT NO 1L161102BH57	TASK NO 04	WORK UNIT ACCESSION NO
11 TITLE (Include Security Classification) (U) EXPERIMENTAL INVESTIGATIONS OF WAVE FRACTURE PHENOMENA IN IMPACTED CERAMIC MATERIALS					
12 PERSONAL AUTHOR(S) S. WINKLER H. SENF H. ROTHENHAUSLER					
13a TYPE OF REPORT FINAL		13b TIME COVERED FROM DEC 87 TO MAY 89		14 DATE OF REPORT (Year, Month, Day) 89-8-10	15 PAGE COUNT 101
16 SUPPLEMENTARY NOTATION					
17 COSATI CODES			18 SUBJECT TERMS (Continue on reverse if necessary and identify by block number)		
FIELD	GROUP	SUB-GROUP	Alumina, High Speed Photography, Shadow Optical Method, Terminal Crack Velocity, Specific Wave Energy, Energy Absorb- tion Mechanism, Crack Nucleation, Fractography		
1102					
1904					
19 ABSTRACT (Continue on reverse if necessary and identify by block number) (U) Experiments have been performed to investigate the fracture behaviour of pressure wave loaded alumina tiles. The waves were produced by impacting steel projectiles at a speed range between 100 and 1200m/s. The investigation of the damage generation phase was made possible by a newly developed special loading and observation arrangement. The tiles were impacted edge on and observed was one of the large surfaces by a photographic high speed technique in combination with the shadow optical method.  The aim was to observe the fracture appearance and, based on this, to understand energy absorbing processes. The results were compared with those of earlier experiments with glass slabs. It was found that alumina behaves quite different than glass. From a fracture mechanics point of view it was most surprising that no distinct terminal crack velocity could be found as was expected and was experienced with glass. Although for certain loading condition the crack velocity seemed to be					
20 DISTRIBUTION/AVAILABILITY OF ABSTRACT <input type="checkbox"/> UNCLASSIFIED UNLIMITED <input type="checkbox"/> SAME AS RPT <input type="checkbox"/> OTIC USERS			21 ABSTRACT SECURITY CLASSIFICATION		
22a NAME OF RESPONSIBLE INDIVIDUAL		22b TELEPHONE (Include Area Code)		22c OFFICE SYMBOL	

DD FORM 1473, 84 MAR

83 APR edition may be used until exhausted  
All other editions are obsolete

SECURITY CLASSIFICATION OF THIS PAGE

19.

terminated, different terminal crack velocities were measured for different situations. The responsible input parameter is assumed to be the specific energy of the pressure wave. Two energy absorption mechanisms were observed: In the regime of a low specific energy, an energy augmentation causes the crack speed to increase while the number of produced cracks remains small and essentially constant. This changes rather abruptly into the opposite when the crack speed exceeds a threshold at about 80% of the correlated wave speed. The number of cracks becomes large, their velocity, however, increases only slightly and seems to approach the wave speed asymptotically.

CONTENT

	PAGE
1. Introduction	1
2. Background	3
3. Experimental Techniques	7
3.1 Loading Devices	7
3.2 Trigger Circuits	8
3.3 High Speed Camera	11
3.4 Optical Method	12
3.5 X-ray arrangement	15
3.6 Loading Arrangements	15
4. PREEXPERIMENTS	17
4.1 Central Impact	17
4.2 Edge On Impact	23
4.3 Testing the Reflection Method	29
5. SPECIMEN PREPARATION	40
6. EXPERIMENTAL RESULTS	42
6.1 Wave And Crack Propagation	42
6.2 Target Recovery	66
7. ANALYSIS OF WAVE AND FRACTURE PHENOMENA	76
7.1 Evaluation of Wave Data	76
7.2 Evaluation of Crack Data	81
7.2.1 Crack velocities	81
7.2.2 Influence of impact area	90
8. DISCUSSION AND CONCLUSIONS	94
9. ACKNOWLEDGEMENT	97
10. REFERENCES	98
11. APPENDIX	100

Accession For	
NTIS GR&I	<input checked="" type="checkbox"/>
DTIC TAB	<input type="checkbox"/>
Unannounced	<input type="checkbox"/>
Justification	
By _____	
Distribution/	
Availability Codes	
Avail and/or	
Dist	Special
A-1	

## 1. INTRODUCTION

The presented work is an attempt to extend earlier work on energy consumption effects in dynamically loaded glass targets to ceramic materials. These materials gain an increasing importance for protection purposes in ballistic applications due to their unexpectedly large ballistic resistance against the impact of kinetic energy projectiles. It is assumed that these properties are a consequence of a non-linear energy absorption effect which has not yet been completely investigated and understood. New informations on the energy sink are expected from the investigation of wave propagation and fracture occurrence within the dynamically loaded fragmenting material.

Initially assigned transparent sapphire samples were not available in time, so the experiments were performed with alumina tiles all of the same batch with the desired dimensions and probably almost the same material parameters. This material was used to learn about how to prepare surfaces of an opaque, non-metallic material for optical purposes and how to work with this material.

An optical method - high speed photography with the application of the shadow optical method - is the main research technique during this work. The material samples are impacted by a projectile or a bullet. Waves and fractures occur within the sample and their appearance is photographed and measured.

It was expected and also experienced during this work that with the step from glass to ceramics two main features changed significantly:

- Ceramic materials exhibit sonic velocities about twice of those of glasses. Consequently, electronic aids often reach their limits with respect to time resolution and, sometimes, have to be improved.

- The material is opaque and it is not possible anymore to observe wave and fracture phenomena inside the targets by transmitted light as before with glass. With the applied optical method in reflection surface phenomena only can be seen and these have to be understood with respect to the originating events inside the material.

In this report a brief review (chapter 2, BACKGROUND) recapitulates findings of earlier work which serve as a starting platform for the current research.

The experimental technique mainly applied in this research is sketched in chapter 3, EXPERIMENTAL TECHNIQUES. This includes loading devices, improved electronic aids, and the shadow optical method combined with high speed photography.

PREEXPERIMENTS are reported in chapter 4. Their purpose was to connect to earlier work and to test new methods, e.g. the shadow optical method in reflection under new and difficult conditions.

SPECIMEN PREPARATION is described in chapter 5.

Current results are reported in chapter 6, EXPERIMENTAL RESULTS, analysed in chapter 7, ANALYSIS OF WAVE AND FRACTURE PHENOMENA, and discussed in chapter 8, DISCUSSION AND CONCLUSIONS.

A ceramographical description of the material used in this work is given in the APPENDIX.

## 2. BACKGROUND

In previous experiments and numerical simulations [1, 2] the response of different glass materials to impact loading was investigated. Nine series of experiments were performed, eight with different glasses and one with a

material	$\rho$ kg/m <sup>3</sup>	E GPa	$\nu$	HV	$c_L$ m/s	$Z = \rho c_L$ kg/(m <sup>2</sup> s)
Floatgl.	2 500	-	-	680	5 860	14.7*10 <sup>6</sup>
SF6	5 180	56	0.248	407	3 595	18.6*10 <sup>6</sup>
SF14	4 540	65	0.235	465	4 091	18.6*10 <sup>6</sup>
F6	3 760	57	0.231	455	4 196	15.8*10 <sup>6</sup>
SKN18	3 640	88	0.296	689	5 673	20.6*10 <sup>6</sup>
FN11	2 660	84	0.23	710	6 051	16.1*10 <sup>6</sup>
K5	2 590	71	0.227	584	5 624	14.6*10 <sup>6</sup>
PK3	2 590	84	0.207	680	6 030	15.6*10 <sup>6</sup>
Zerodur	2 530	91	0.24	750	6 511	16.5*10 <sup>6</sup>
Steel	7 800	201	0.30	1019	5 850	45.6*10 <sup>6</sup>
WC	14 900	576	0.22	1630	6 650	99.1*10 <sup>6</sup>

Table 1 Data of the material used in earlier research (after [1, 2]); data for steel and tungsten carbide (WC), the bullet material, are taken from [6], Tables 2 and 3

glass ceramic (Zerodur). The targets were impacted by bullets fabricated from tungsten carbide (WC). A constant impact velocity of  $v_p = 1060$  m/s was used. These materials differed by their material constants according to Table 1. The symbols are  $\rho$  = mass density,  $E$  = Young's modulus,  $\nu$  = Poisson's ratio, HV = Vickers hardness,  $c_L$  = longitudinal wave velocity, and  $Z$  = acoustic impedance.

Results are given in the graphs of Figures 1 to 3. Investigated was the ballistic resistance of the materials which is characterized by the normalized residual velocity,  $v_R/v_p$  ( $v_R$  projectile velocity after perforation,  $v_p$  impact velocity). Those experiments were carried out in two different ways: with a constant area density  $\rho_F$  of the target material (i.e. varying thickness of the target), symbol (x), and with targets (diameter 150 mm) of constant thickness  $d$ , symbol (●).

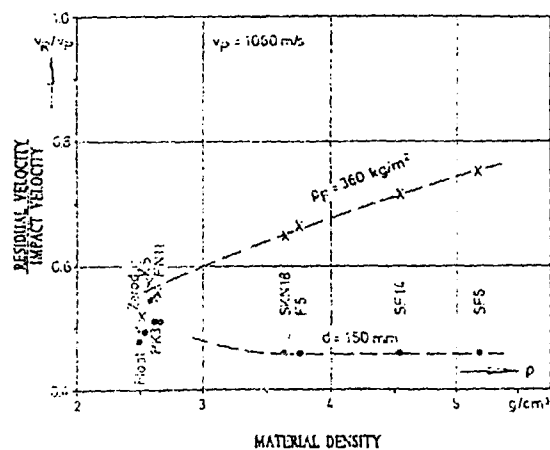


Fig.1 Normalized residual velocity vs. material density of the target material (x: constant area density, ●: constant plate thickness) (after [1, 2])

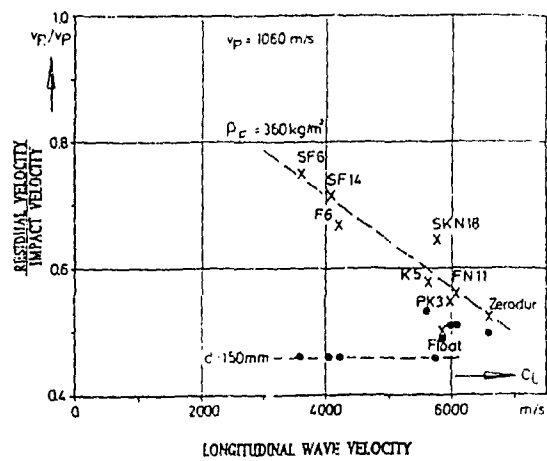


Fig. 2 Normalized residual velocity vs. wave velocity of the target material (x: constant area density, ●: constant plate thickness) (after [1, 2])

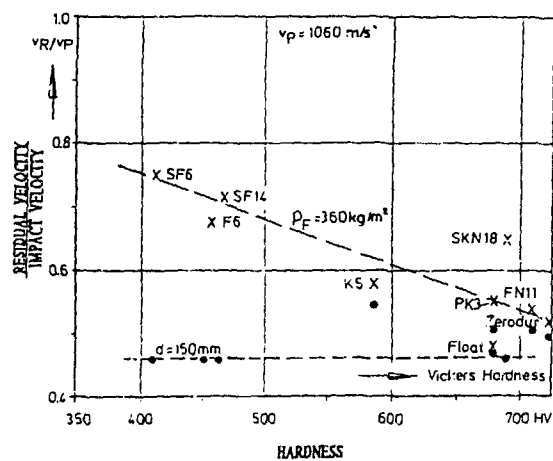


Fig. 3 Normalized residual velocity vs. Vickers hardness of the target material (x: constant area density, ●: constant plate thickness) (after [1, 2])

Further and more general results of these series of glass experiments can be summarized as follows:

- With glass targets bullets made out of WC behave rigid. Usually, they are neither fragmented nor eroded and maintain their dimensions when penetrating the glass targets.
- The structure of the target (homogeneous or laminated glass blocks) does not significantly influence the ballistic resistance.
- Targets with a constant area density (i.e. varying thicknesses) show increasing ballistic resistance when the density decreases and sound wave velocity and hardness increase.
- Targets with a constant thickness have the same ballistic resistance.
- These four experimental results could also be verified by a numerical simulation using the 2D/3D Lagrange code DYMAS/L.
- The behaviour of a hypothetical material calculated with this code by using the density  $\rho$  of glass SF6 (Table 1) and all the other parameters taken from glass FN11 (Table 1) resulted in a residual velocity  $v_R = 0.14 v_P$  (loading conditions remain unchanged). This differs considerably from comparable results with real materials (Table 1 and Figs.1 to 3) and is close to the behaviour of ceramic materials.
- No hint was found for a contribution of secondary cracks generated in the pressure regime of the shock wave [3] to the failure behaviour of the glass targets, neither in experiments nor with numerical simulations.

All these results show that with glass not just one unique physical (static) property determines the ballistic performance of a material. It is rather a group of parameters which has to be changed to improve the ballistic performance. This is obviously also true with ceramics, which was concluded by Viechnicki and coworkers [4, 5].

### 3. EXPERIMENTAL TECHNIQUES

#### 3.1 Loading Devices

The impact experiments are performed with the use of a gas gun and a powder gun, depending on the range of the impact velocity. The gas gun is used with impact velocities below 400 m/s and the powder gun above this value up to about 1500 m/s. Testing the optical method with mirrored ceramic samples was achieved with a 4.5 mm bore air rifle and a bullet speed of about 200 m/s. With some of the main experiments a 50 mm bore gas gun was used. With this machine very precise impacts can be produced since the target can be fixed right at the muzzle of the barrel. The projectile then is still guided by the barrel during the impact event. For the powder gun two different barrels were used, one with an inner diameter of 12.7 mm and another one with a 20 mm bore. Because of the very high expansion speed of the opaque propellant cloud in the vicinity of the muzzle it is not possible to fix the target near to the muzzle. A several metres free flight distance is, therefore, necessary, but makes it difficult to achieve a reproducible and precise impact.

Two types of projectiles were used with the 50 mm gas gun, flyer plates 10 mm thick and 49 mm in diameter made from ARMCO iron and ball-like impactors for a pointed impact with 10 mm diameter fixed on a flyer plate. In both cases the impactors were glued on a light and hollow aluminum sabot. The projectiles for the powder gun (diameters 12.7 mm and 20 mm) were fabricated from steel for the main experiments. Their masses were 12.7 g and 50 g. Also in this case two bullet shapes were used, one with a blunt and the other one with a conical nose.

### 3.2 Trigger Circuits

The impact velocity was measured with one or two light barriers which are interrupted by the travelling projectile prior to impact. The principle is to count the time the projectile needs to pass a certain basic length. If only one light beam is used, the interruption time must be determined, i.e. the length of the projectile is the base of the speed measurement and must, therefore, be known. An interrupted light beam or a light grid was in some cases also used as a trigger device for starting the high speed camera a few microseconds before impact.

Light beams - e.g. laser beams - do not exhibit a well defined diameter. The intensity distribution across the diameter is often gaussian-like and the intensity can fluctuate somewhat with time. A fixed trigger threshold for the light pulse as commonly used has the consequence, therefore, that the basic length for the velocity measurement or the site of the trigger event is not very well defined. A newly developed sophisticated circuit

matches the trigger threshold to exactly one half of the intensity of the light beam right before the interruption, and avoids, therefore, scatter by fluctuating light and determines the trigger sites exactly to the center of the beam. The principles of this circuit are shown in Fig.4.

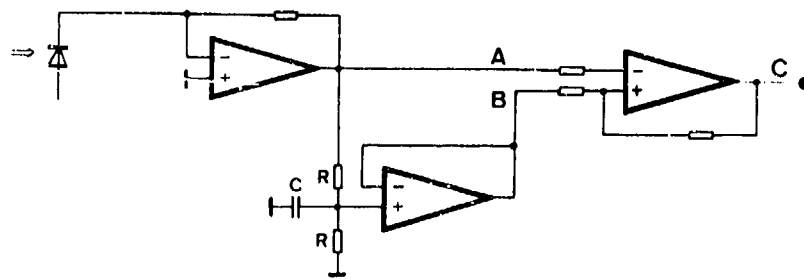


Fig.4 Circuit diagram of an automatically centering trigger device

The optical signal is picked up by a PIN-diode and transferred into a voltage signal A. Half of the signal is stored in a capacitor C with an appropriate time constant. This is labeled "B" in Figs.4 and 5 and used as a reference signal. If a projectile then is going to cover the beam the decreasing original signal A passes the stored signal B as is shown by the oscilloscope traces of Fig.5. At this instant the comparator forms the trigger signal C (Figs.4 and 5).

Another malfunction of light beam triggering can occur if the air shock wave produced by the flying projectile is not attached to it but travels with a faster velocity at an

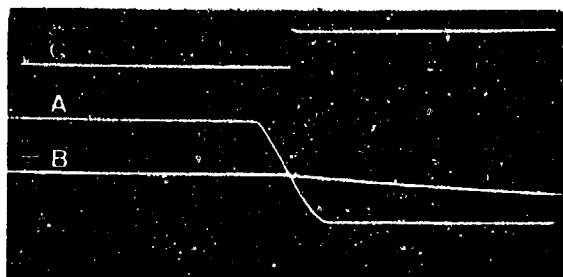


Fig.5 Oscillograms of the signals A, B, and C of Fig.4

increasing distance to the projectile. The shock wave can be able to deflect the light and simulate a passing projectile. This happened with the 50 mm gas gun with velocities in the 200 m/s range. In these cases a trigger contact solved the problem with a pair of contact wires being short-circuited by the flyer plate at a certain distance  $x$  in front of the target for a pretrigger. The pretrigger time  $t_{-}$  is calculated to be

$$t_{-} = x/v_p \quad (1)$$

with  $v_p$  being the impact velocity. An impact velocity of 100 m/s and a distance  $x = 1$  mm produces a pretrigger of  $t_{-} = 10 \mu\text{s}$ . The utility of a well defined pretrigger is obvious for the registration of electronic zero-signals or a zero-picture with the high speed camera. The circuit of this contact trigger device is shown in Fig.6.

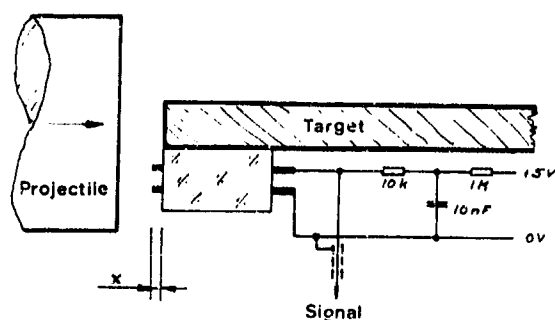


Fig.6 Contact trigger device

### 3.3 High Speed Camera

The main tool for the reported investigations was a high speed camera of the Cranz-Schardin type. This is a 24 spark camera with the sparks being fired one after the other by a precise quartz generator and a minimum picture separation time, i.e. a time resolution, of one microsecond. Spatial picture separation is achieved by a concave mirror which images the plane containing the 4 \* 6 spark array onto a plane containing the 24 lenses of the camera being arranged in the same way. This principle of the camera requires the specimen being an optical part of the ray tracing, this is either a window in the case of transparent specimen material or a mirror in the case of an opaque specimen material. Only the effect of interest, say a moving bullet, a wave, a crack, or any other distortion, shall become visible.

A typical experiment is sketched in Fig.7 with a mechanically loaded notched transparent bend specimen as an object. If, at the critical load, the notch tip becomes

instable a light beam traversing the specimen is interrupted by the propagating crack and consequently triggers the camera in order to photograph the propagating crack. The light rays of the sparks are affected only by the crack and by loading effects in the vicinity of the crack tip but not by the remaining parts of the specimen.

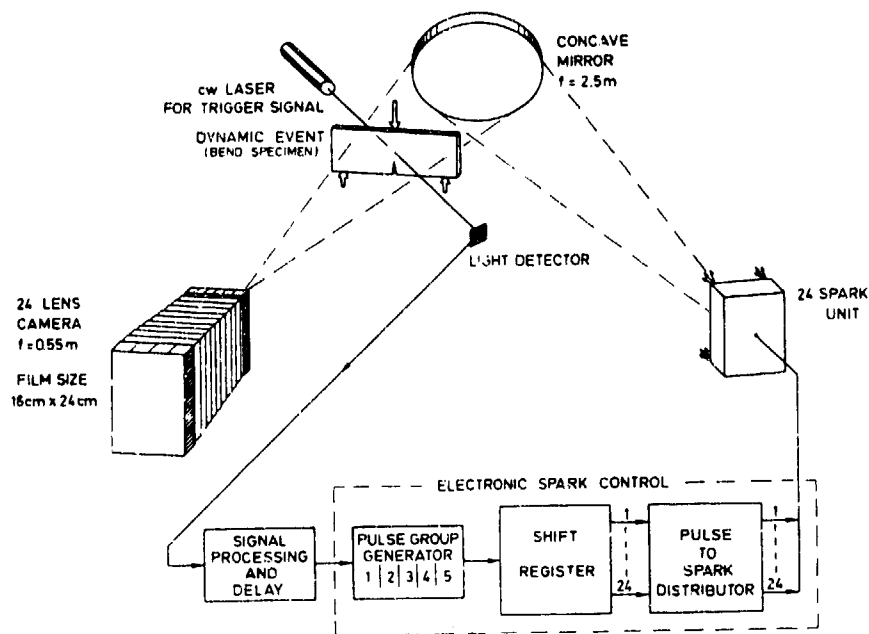


Fig.7 Application of the Cranz-Schardin camera in a transmission arrangement

### 3.4 Optical Method

The application of the Cranz-Schardin high speed camera requires the additional application of an optical method to

visualize the mechanical effect of interest. Examples of these methods are

- shadow photography (silhouette imaging), camera focussed onto plane of object; example: flight of a bullet;
- shadow optical method, camera focussed onto a plane different from the object plane in order to photograph a shadow pattern formed by deflected light;
- shadow optical method of caustics, a special case of the previous method accompanied with the occurrence of stress concentrations (for details see [7]);
- schlieren optical method;
- photo-elastic method, (stress birefringence);

Throughout this work shadow photography and the shadow optical method were used both in a special version, these methods in reflection (because of the ceramic specimens being opaque). The shadow optical method utilizes the deflection of light by movements (i.e. tilts) of the reflecting sample surface caused, for instance, by internal mechanical pressure. The deflected light forms shadow spaces outside the sample. Cross sections of them, the shadow patterns, can be photographed by the camera. For this purpose the camera must be focused onto this plane which may be called a reference plane with distance  $z_0$  from the object plane (the sample plane). The size of the shadow pattern, i.e. the sensitivity of the method, depends on the distance  $z$  which must be matched to the problem. The optical arrangement used with the experiments reported here is shown in Fig.8.

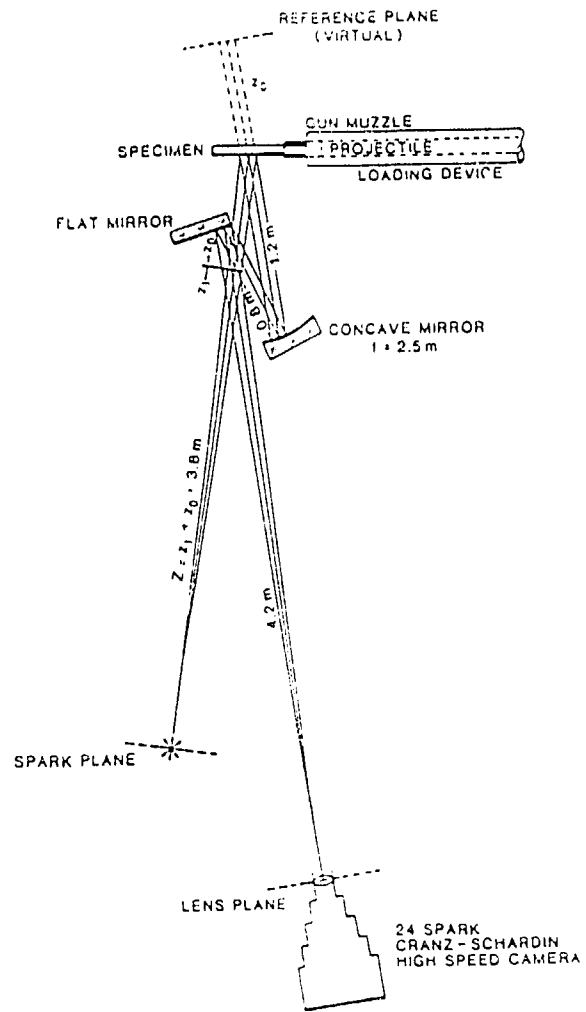


Fig.8 Camera arrangement for the shadow optical method in reflection

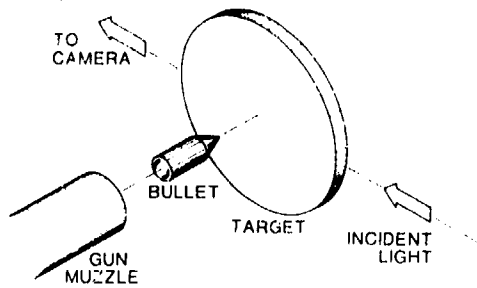
### 3.5 X-ray Arrangement

The X-ray arrangement consists of a 4 channel 300 kV FIELD EMISSION equipment. The distance between X-ray tubes and target is 1 m and between target and film about 0.2 m. The radiation axis is perpendicular to the impact direction. With this equipment single flash photography or cinematography can be performed. The purpose for the application in this research was to study the quality of projectile impact and to get informations on the deformation of projectiles during penetration within fragmented targets or debris clouds which are opaque for optical radiation.

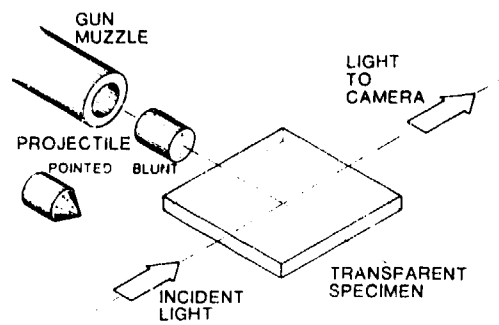
### 3.6 Loading Arrangements

Three different loading arrangements were used for the work reported here. These are illustrated in Fig.9. They either differ in the impact mode or in the observation mode. Pre-experiments (chapter 4) were performed in the starting phase with the arrangement shown in Fig.9a with the specimen loaded centrally for perforation experiments. Edge on loading combined with up-side viewing (Fig.9b) was also used in pre-experiments in order to study details of the impact event. Fig.9c shows the arrangement which was used to photograph wave propagation and damage processes.

(a) central loading



(b) edge on loading



(c) edge on loading

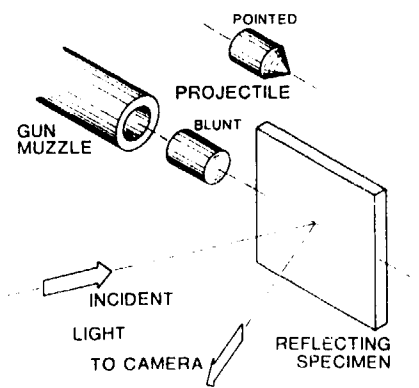


Fig.9 Loading arrangements

#### 4. PREEXPERIMENTS

##### 4.1 Central Impact

Impact experiments have been performed to study the difference of damage processes in glass and ceramic. The shape of the targets was circular with a diameter of 150 mm and a thickness of 10 mm. They were impacted at the centre point (Fig.9a) under identical conditions by pointed tungsten carbide projectiles, length 41 mm, diameter 13 mm, mass 68.9 g, striking velocity  $v_p = 1060$  m/s.

Two examples of the photographic series of the penetration event are shown in Fig.10 for a glass target and in Fig.11 for a ceramic target. Some results taken from these

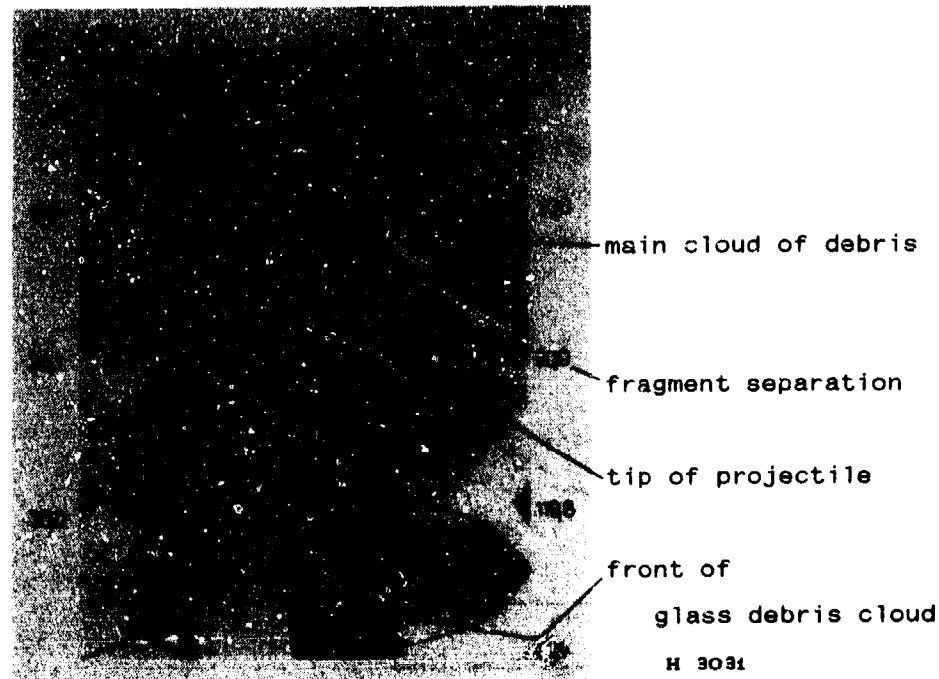
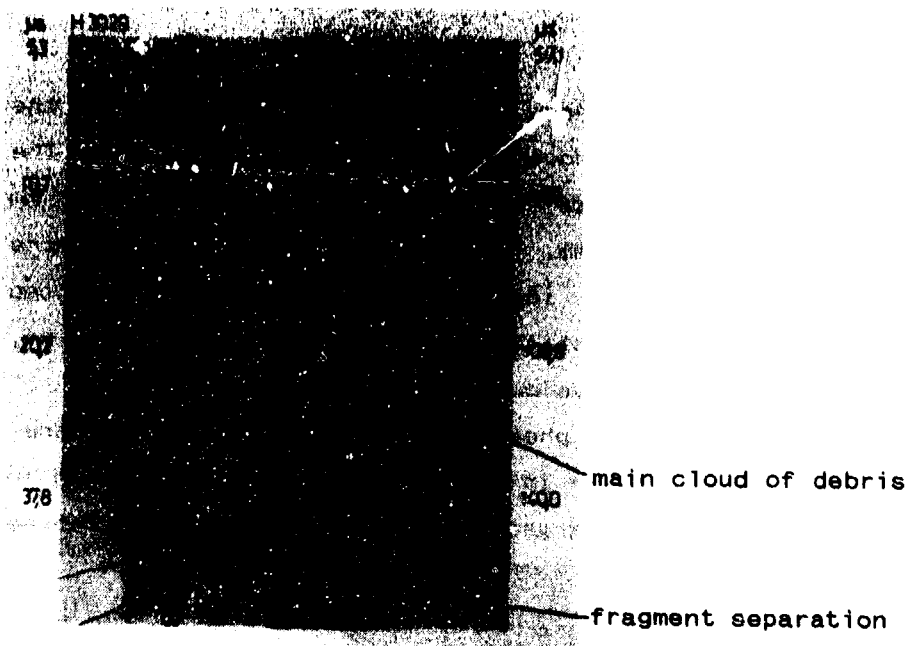


Fig.10 A pointed WC bullet perforating a crown glass target (thickness 10mm)



H 3029

Fig.11 A pointed WC bullet perforating an alumina target (thickness 10mm)

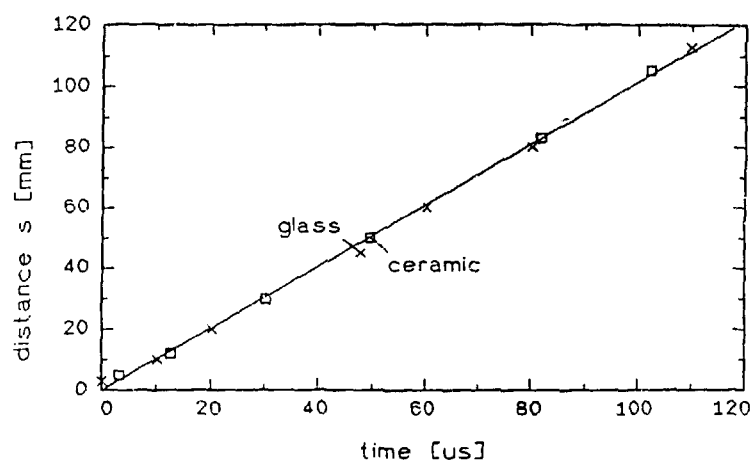


Fig.12 Axial movement of the bullet (Fig.10) or its fragments (Fig.11)

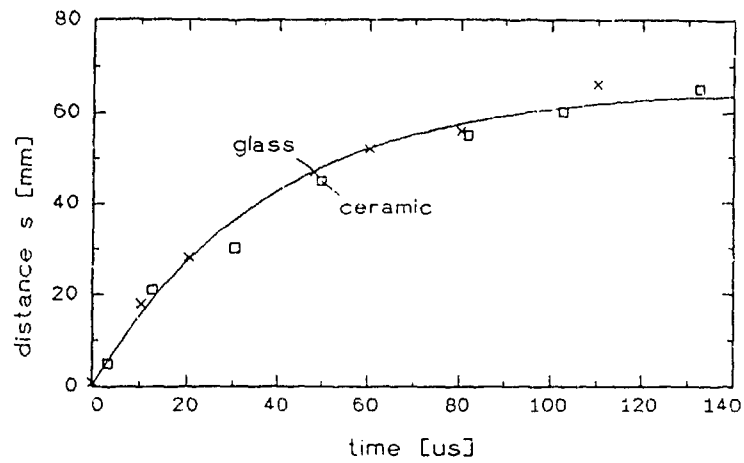


Fig.13 Radial expansion of the main material cloud

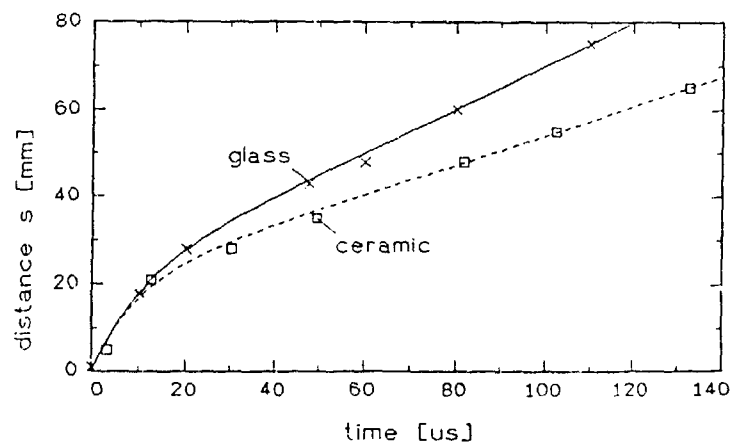


Fig.14 Radial expansion of fragment separation (target material) from the rear surface

figures are presented in the graphs of Figures 12, 13, and 14. From Fig.12 must be concluded that after perforation the bullet (Fig.10) or its fragments (Fig.11) travel with the same residual velocity,  $v_R = 0.94 v_P$ , for both target materials.

Fig.14 shows that the radial separation movement of the debris from the rear surface is slightly faster with glass than with ceramics. The movement in axial direction, on the other hand, is slower with the glass due to air drag (Fig.10).



Fig.15 Moving fragments of a WC bullet after perforating a 10mm alumina target; X-ray flash shadowgraph

With all these experiments the tungsten carbide projectiles either survived the experiment almost unhurt or were completely destroyed (Fig.15). This phenomenon of the bullet, fragmenting or not when perforating a target, depends on the target material. With glass as the target

material the bullet, remained undamaged, with alumina not.

This can be understood by an estimation of the stresses produced in bullet and target) by the impact generated shock waves. The pressure  $\sigma$  of a shock wave is determined by the shock impedances (approximately equal to the acoustic impedance  $Z = \rho c_L$ ) of the involved materials, i.e., the target and the projectile material (see eq.(2)). This can be illustrated by a  $(\sigma, v)$ -state diagram (Fig.16), which shows the states prior to impact of the target (1) in the origin of the diagram ( $\sigma = 0, v = 0$ ) and of the bullet (2) on the horizontal axis ( $\sigma = 0, v = v_P$ ). The states of the impacted materials, determined by the stress  $\sigma_A$  of the state and by the particle or mass velocity  $v_A$  within the

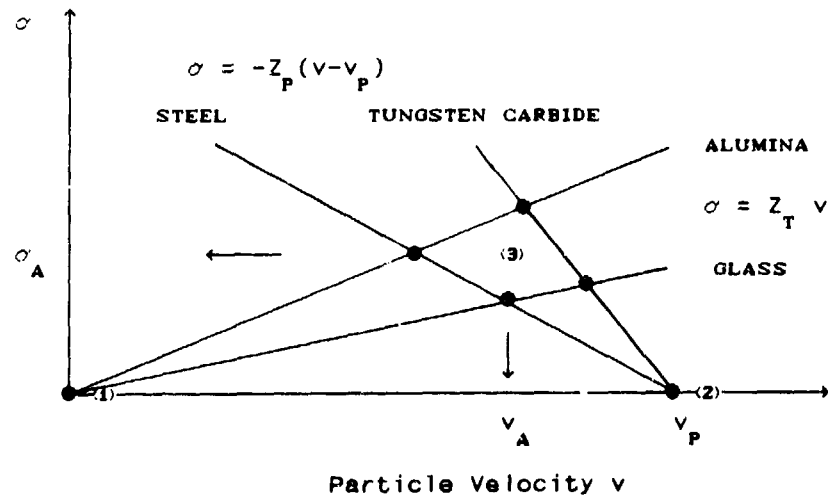


Fig.16  $(\sigma, v)$ -state diagram for a glass and an alumina target, both impacted by a tungsten carbide and a steel impactor

stressed volume, are given by the intersection points (3) of the Rayleigh lines of the involved materials. The slopes of the Rayleigh lines are determined by the acoustic impedances of the materials. It can be seen that for ceramics with the larger acoustic impedance the common stresses produced in impactor and target are larger than with a glass target. A second line shows the same situation for a steel impactor. For steel  $Z = 45 \cdot 10^6 \text{ kg}/(\text{m}^2\text{s})$  (Table 1). This is about one half of that of tungsten carbide. Consequently, the corresponding state parameters are somewhat below the data for tungsten carbide.

The state coordinates of the diagram of Fig.16 are approximately given by eqs.(2a) and (2b):

$$(a) \sigma_A = \frac{Z_T * Z_P}{Z_T + Z_P} v_P, \quad (b) v_A = \frac{Z_P}{Z_T + Z_P} v_P \quad (2)$$

with the indices T and P for target and projectile, respectively. The expression for  $\sigma_A$  can be used to compute quantitative pressure data:

The acoustic impedances  $Z = \rho * c_L$  of glass are given in Table 1. The largest value is  $Z = 20 \cdot 10^6 \text{ kg}/(\text{m}^2\text{s})$ . With the data  $\rho$  and  $c_L$  of alumina given in the appendix an acoustic impedance  $Z = 40 \cdot 10^6 \text{ kg}/(\text{m}^2\text{s})$  is calculated. The data of tungsten carbide (from [6]),  $\rho = 14\ 900 \text{ kg}/\text{m}^3$  and  $c_L = 6650 \text{ m/s}$ , yield  $Z = 100 \cdot 10^6 \text{ kg}/(\text{m}^2\text{s})$ .

With this follows for the pressure of the waves produced when impacted by a tungsten carbide bullet at 1060 m/s

$$\sigma_{A, \text{GLASS}} = 18 \text{ GPa}$$

and

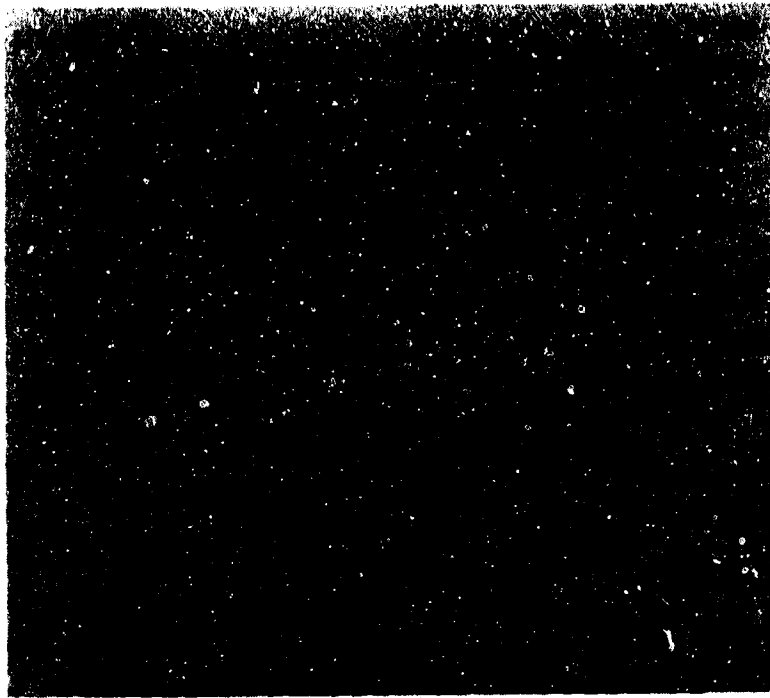
$$\sigma_{A, \text{ALUMINA}} = 30 \text{ GPa.}$$

These two stresses differ by almost a factor of two. In both cases the targets were fractured. Obviously, these pressures exceed the strengths of the target materials. The tungsten carbide projectile, however, was only fractured with the alumina target, not with the glass targets. It must be concluded, therefore, that the fragmentation threshold (the ultimate strength of tungsten carbide) lies somewhere in between these two values, 18 and 30 GPa.

#### 4.2 Edge On Impact

The reproducibility of wave and fracture phenomena depends on the accuracy of the impact event. The energy transfer, for example, is sensitively controlled by the way the contact takes place. Difficulties can arise with powder guns. At the muzzle, the opaque propellant cloud is faster than the projectile and disturbs the observation. A certain free flight distance is, therefore, necessary to sufficiently separate projectile and cloud. This free flight period, however, can be the reason for problems concerning the precision of the impact event, with blunt as well as with pointed bullets.

Some attention, therefore, was focused on this event. With the arrangement shown in Fig.9b optical and X-ray high speed photography was applied. An experiment with simultaneously applied optical and X-ray photography is shown in Figs.17a and b. The glass target was impacted by a blunt steel bullet ( $v_p = 1002$  m/s). The loading arrangement was that of Fig.9b. The picture interval times of the optical photographs are shown in the figure (Fig.17a). The X-ray shadowgraph of this experiment was taken in an

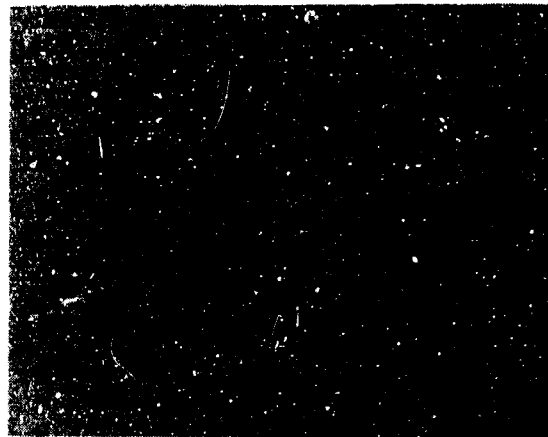


(a)

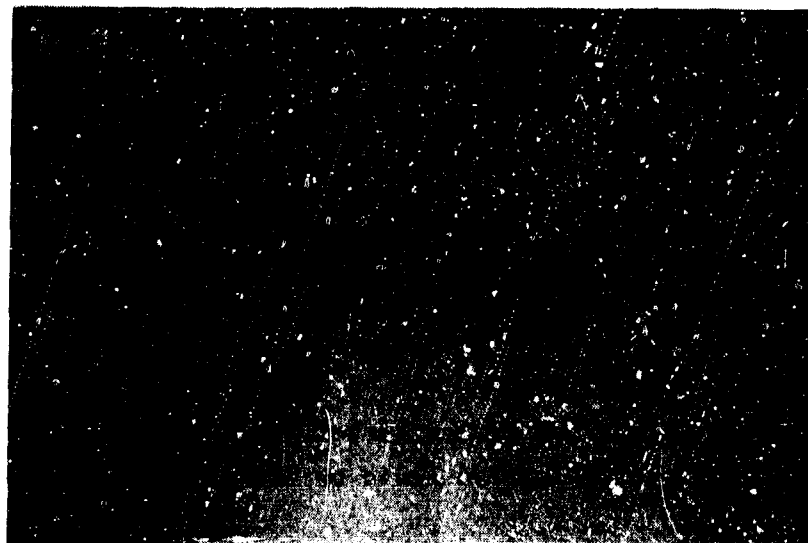


(b)

Fig.17 Symmetrically impinging blunt bullet on glass slab  
(a) optical shadowgraphs (arrangement Fig.9b)  
(b) X-ray flash shadowgraph (arrangement Fig.9c)



(a)



(b)

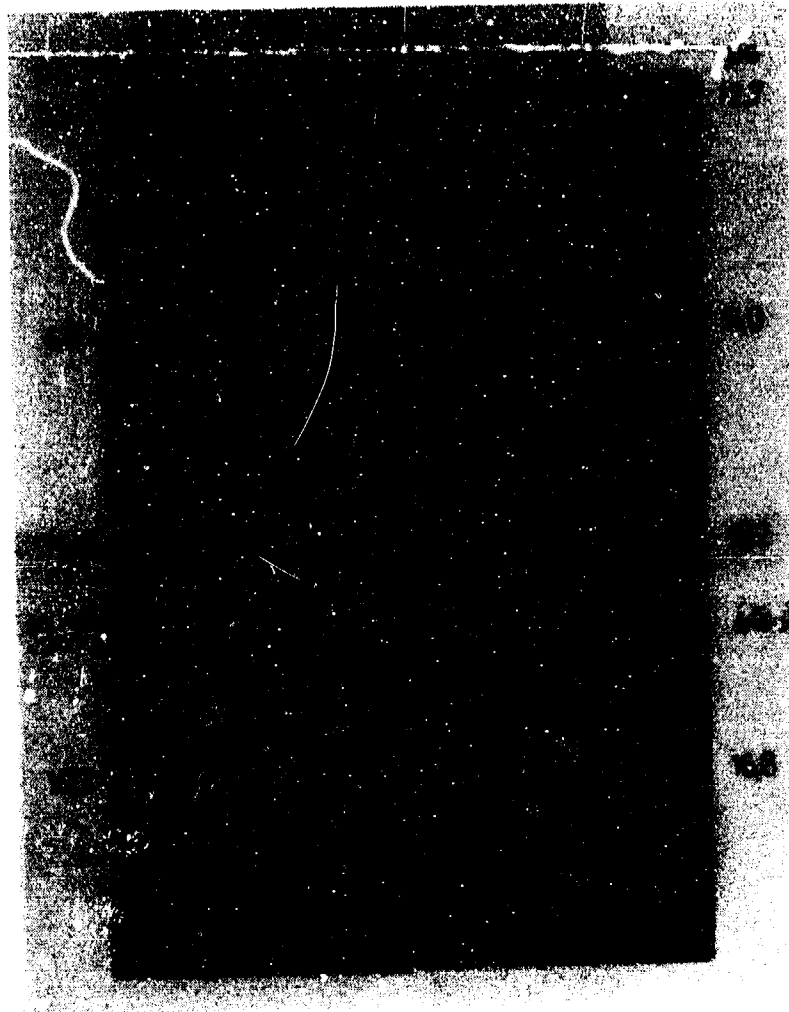
Fig.18 Symmetrically impinging bullets on glass slabs  
(a) X-ray flash shadowgraph (arrangement Fig.9b)  
(b) optical shadowgraph (arrangement Fig.9b)

arrangement similar to Fig. 9c. It shows cratering of the glass target and deformation of the penetrating bullet after 18.9 $\mu$ s. The shadow areas on the sides and in front of the bullet are due to the expanding fine debris of the glass rather than to shock compression. This observation method is not sensitive for cracks and voids within the target.

Fig.18 shows two more experiments with satisfactory impact situations at very high impact velocities,  $v_p = 1582$  m/s (Fig.18a) and  $v_p = 1412$  m/s (Fig.18b).

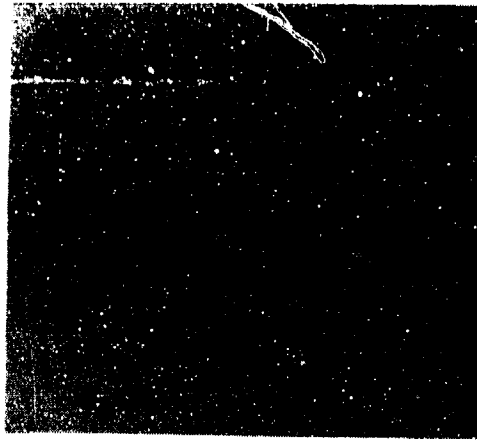
Experiments with unsatisfactory oblique impacts are shown in the next two figures, Fig.19 and Fig.20a and b. In the two optical shadowgraphs air shock waves due to the Poisson effect can be seen on each side of the target. The unsatisfactory impact situation is demonstrated by their asymmetry. The degree of asymmetry can also be seen from the debris cloud not being symmetrical anymore. X-ray photography shows the plastic deformation of the bullet being asymmetrical if the bullet hits the target under an oblique angle.

These experiments caused a rearrangement of the gun-target set-up and resulted in an improvement of the impact precision: the muzzle-target distance was reduced and the bullet fabrication could be improved.

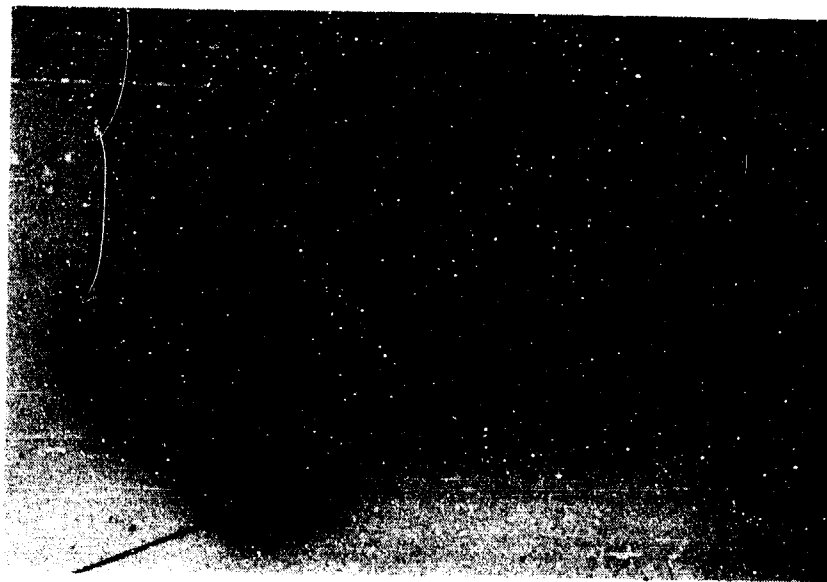


H 3269

Fig.19 Asymmetrically impinging bullet on a glass slab



(a)



(b)

Fig.20 Asymmetrically impinging bullets on glass slabs  
(a) X-ray flash shadowgraph (arrangement Fig.9b)  
(b) optical shadowgraph (arrangement Fig.9b)

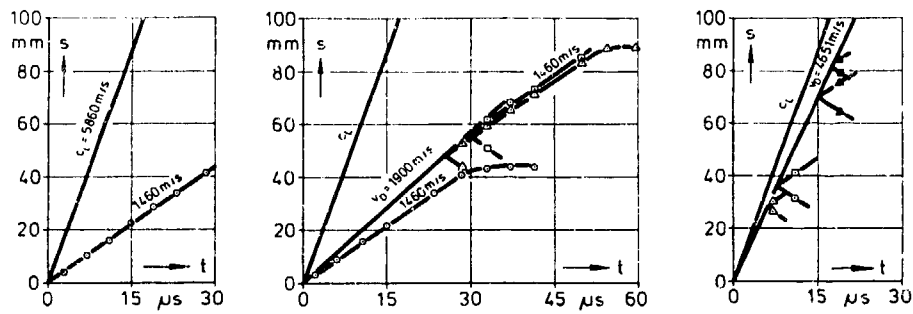
#### 4.3 Testing the Reflection Method

With the experiments performed earlier [3] on glass slabs using the shadow optical method in transmission (see Fig.21) material failure could easily be observed and measured since interpretation of optical effects was straight forward:

At the impact site a black area is produced and this was interpreted as the material being damaged into a very fine debris. Much of the initial energy is consumed by this process. After this starting period a great number of single, radial cracks develop and propagate all with the same velocity indicated by the circular shape of the crack front. This turned out to be the terminal crack velocity of glass, 1460 m/s, well known from fracture mechanics. This crack tip front is, obviously, far behind the longitudinal wave front ( $\approx 5860$  m/s) or the transversal wave front ( $\approx 3450$  m/s).

An increasing number of additional cracks occur in front of the primary cracks with an increasing impact velocity, i.e., energy density in the specimen (Fig.21b and c). These "secondary cracks" emanate from nuclei activated in the stress field behind the longitudinal wave front and expand radially in both directions, towards the impact site and away from it with terminal crack velocity, 1460 m/s (Fig.21b). This behaviour is even more pronounced with blunt bullets, the number of nuclei increases significantly (Fig.21c). The large impact area is capable to transfer much more energy into the target.

These situations are demonstrated by the two wave diagrams of Figs.21a and c. No nucleation was seen with the



(a) pointed bullet, (b) pointed bullet, (c) blunt bullet,  
 $v_p = 548\text{m/s}$        $v_p = 825\text{m/s}$        $v_p = 785\text{m/s}$

Fig.21 Three experiments with glass targets and the optical transmission technique (from [3])

slower pointed bullet of Fig.21a. The connection of all nucleation events in the experiment of Fig.21c results in a straight line, the slope of it forming what was called "damage velocity  $v_D$ ". This is a very high one in the experiment of Fig.21c,  $v_D = 4651$  m/s. This phenomenon, the generation of additional cracks by activated crack nuclei, is the special damage mechanism observed in glass. One parameter for describing this effect was considered to be the "damage velocity  $v_D$ ".

An additional effect in the experiment of Fig.21c is the visualization of waves. Longitudinal and surface waves are photographed. This was achieved with the application of the "shadow optical method", i.e. with the camera focused onto a reference plane different from the object plane (see section 3.4, page 12 ff).

Difficulties were expected with the interpretation of the shadow optical photographs in reflection. A program was, therefore, started to develop a stepwise transition from the transmission experiments on glass to reflection experiments on glass in order to better understand the reflection experiments with ceramics. The first step was done by using an uncoated (unmirrored) glass slab as a target, in combination with the shadow optical method in reflection and a mirror mounted behind the specimen to reflect the light (# 5517, Table 3, no picture). The result was the same as with comparable experiments in transmission performed earlier [3].

In the next step this mirror was omitted, so that one part of the light was reflected from the rear surface and

another part from the front surface of the transparent specimen. Also in this case the light reflected at the back face had to traverse the specimen twice, so that this transmission part was still dominating. This experiment is shown in Fig.22. Even in this case the clear and easy to understand pictures were obtained.

In a third step front face coated glass slabs were used in reflection. These experiments should be close to those with the opaque ceramic material, and should, in comparison to the preceding tests, show the capability of the optical method in reflection to make fracture visible.

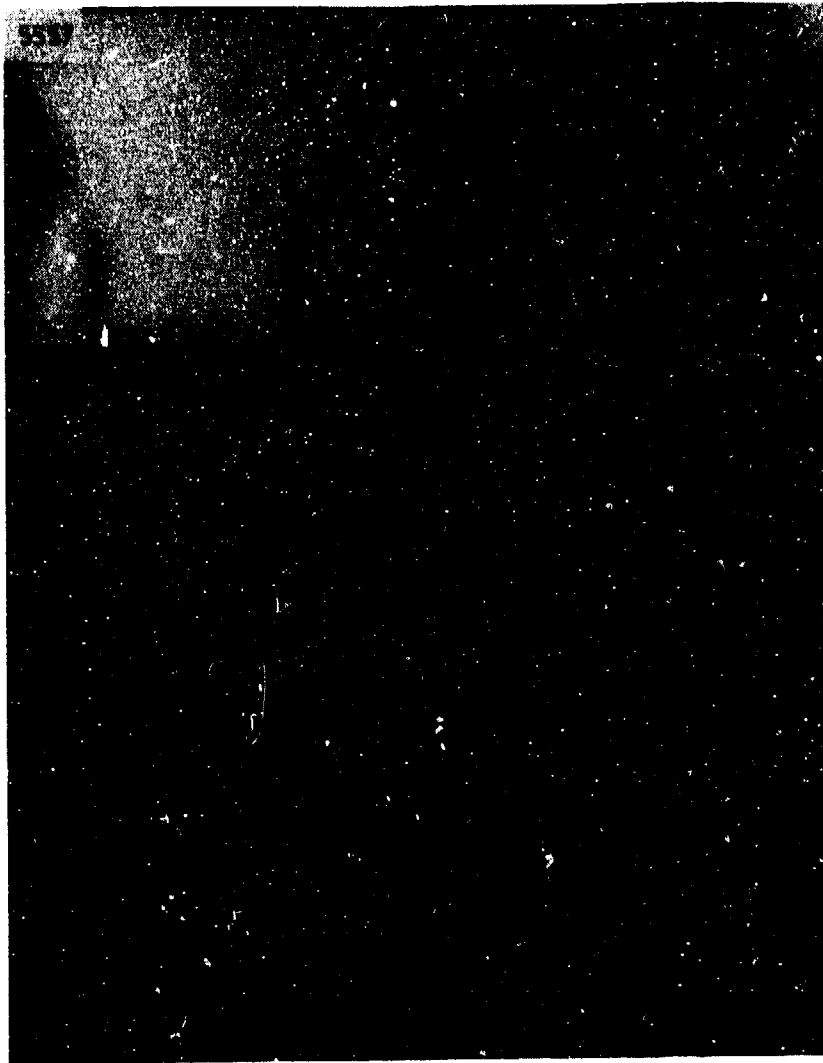
Figs.23 and 24 show two experiments with front face mirrored targets and pointed bullets but different impact velocities. Wave and fracture phenomena can be seen (for data see Table 2, p.38). The observed waves seem to be surface (Rayleigh) waves rather than transverse waves,  $c_{obs} = c_R$ . An analysis given later in section 7.1 (p.76ff) supports this assumption. Fracture events are less easy to understand and evaluate than with the shadow optical method in transition and this becomes worse with increasing impact velocity.

Very fast blunt bullets were used with the experiments of Figs.25 and 26. The target of Fig.25 was not coated with an aluminum layer, neither at the front nor at the back face. The target of Fig.26 was front face coated (for data see Table 3, p.38). The waves seen in both figures have been identified to be longitudinal waves. It is more difficult to identify cracks in these two figures. Deciding between waves, cracks, and a tilted or otherwise disturbed surface is not possible if only a black area can be seen.



5528

Fig.22 Glass slab impacted by a pointed bullet (749 m/s);  
observation in reflection; unmirrored surfaces



5557

Fig.23 Glass slab impacted by a pointed bullet (484 m/s);  
observation in reflection; front surface coated  
with aluminum



5566

Fig.24 Glass slab impacted by a pointed bullet (655 m/s);  
observation in reflection; front surface coated  
with aluminum



5590

Fig.25 Glass slab impacted by a blunt bullet (1076 m/s);  
observation in reflection; unmirrored surfaces



5532

Fig.26 Glass slab impacted by a blunt bullet (1025 m/s);  
observation in reflection; front surface coated  
with aluminum

shot #	$v_p$ m/s	$z_o$ m	$c_L$ mm/ $\mu$ s	$c_{obs}$ mm/ $\mu$ s	$v_c$ mm/ $\mu$ s	$v_D$ mm/ $\mu$ s	f-r $\mu$ s	remarks
5519*	368	0.75	-	-	-	-	2	uncoated
5520*	411	0.75	-	-	-	-	2	uncoated
5557	484	0.75	-	3.0	-	1.66	2	
5564+	599	0	-	-	-	-	2	uncoated
5527	611	0	-	-	1.46	-	4/2	uncoated
5566	655	0	-	3.0	-	1.82	2	
5526	677	0.75	-	4.17	-	1.6	4	uncoated
5565	698	0	-	3.15	1.46	-	2	uncoated
5528	749	0	-	-	1.46	-	4/2	uncoated

Table 2 Glass experiments; pointed projectiles

(\*: Trigger failure, +: camera did not work)

shot #	$v_p$ m/s	$z_o$ m	$c_L$ mm/ $\mu$ s	$c_{obs}$ mm/ $\mu$ s	$v_c$ mm/ $\mu$ s	$v_D$ mm/ $\mu$ s	f-r $\mu$ s	remarks
5569*	657	0	-	-	-	-	2	uncoated
5517	704	0.75	5.86	-	-	4.5	2	mirror
5516	844	0	-	-	1.46	4.16	5	transm.
5532	1025	0.75	5.86	-	-	4.75	1	.
5529+	1069	0.75	-	-	-	-	4/2	uncoated
5531	1073	0.75	5.86	-	-	4.65	2	
5530	1078	0.75	5.86	-	-	4.46	2	uncoated

Table 3 Glass experiments; blunt projectiles

(\*: Trigger failure, +: camera did not work)

Results of all preexperiments with glass slabs are collected in Table 2 for pointed and in Table 3 for blunt projectiles. Listed are shot number, impact velocity  $v_p$ , reference plane distance  $z_0$ , longitudinal wave velocity  $c_L$ , observed wave velocity (very likely Rayleigh wave)  $c_{obs}$ , velocity  $v_c$  of primary cracks, damage velocity  $v_D$  if there was one, picture separation time (framing rate)  $f-r$ , and remarks.

In order to test the shadow optical method in reflection the crack and damage velocities of Tables 2 and 3 are added to the earlier results [3] in Fig. 27. The new data points indicated by open squares fit quite well to the previous ones. From this is concluded that the reflection method is able to deliver correct results even if the evaluation of the pictures is not always unproblematic.

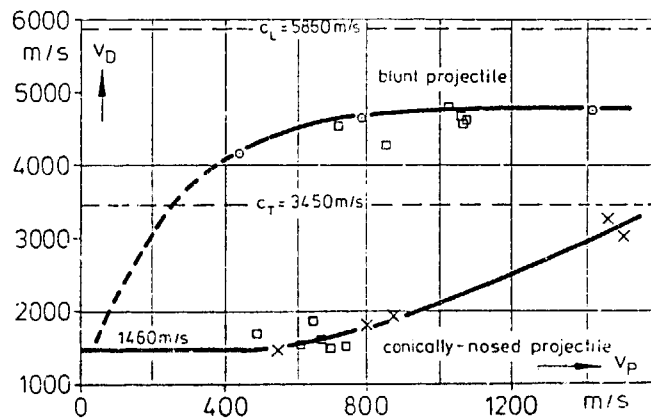


Fig.27 Crack and damage velocities in glass vs. impact velocity, solid curves from [3], new data: open squares

## 5. SPECIMEN PREPARATION

The applied photographic method requires the targets being prepared in a suitable way. One of the large surfaces must be plane and optically polished and exhibit a sufficient reflectivity. Whether the natural reflectivity is sufficient or not depends on the material. With alumina it turned out to be necessary to coat the polished surface with an aluminum layer. This was done by a common vacuum evaporation technique after a careful cleaning procedure.

The material samples were delivered in the desired size, about 100mm \* 100mm \* 10mm, however, flatness and constancy of thickness were not sufficient. All the samples had to be ground using a diamond grinding-wheel or a precision grinding machine.

The next working step, lapping to remove the grinding-scratches (boron carbide as an abrasive on a cast iron wheel), turned out to be extremely time consuming because it was difficult to maintain the flatness of lapping wheel and sample to match the flatness of the succeeding polishing wheel. The polishing procedure was done by diamond powder (2-3 $\mu$ m) in an alcohol-water solution on a rotating tin-wheel. This method has the advantage of not changing the degree of flatness of the wheel seriously with time. It works, therefore, almost automatically. For this reason the intermediate lapping step was mostly omitted later on. However, the polishing time from the state of grinding was quite large. Several hundred hours (typically 400 hours) were necessary to obtain a sufficiently smooth surface. With the available machine

four samples can be prepared at the same time. Currently it is planned to install an additional polishing machine which uses a coarser diamond powder to reduce the working time by a two step polishing procedure.

Unfortunately, some targets were not polished very well. The surfaces show scratches and polishing traces which could hardly be seen by the naked eye. The sensitive shadow optical method, however, makes them visible. Obviously, the quality of the polishing wheel decreased with time. To save time it was decided not to extend the polishing time or to maintain the wheel from time to time since an improvement of the specimen surfaces would not have improved the quality of the data.

## 6. EXPERIMENTAL RESULTS

### 6.1 Wave and Crack Propagation

Data and results of the experiments done with alumina are collected in Table 4 for pointed projectiles and in Table 5 for blunt projectiles. Listed are shot number, impact velocity  $v_p$ , distance of the reference plane  $z_0$ , velocity  $c_L$  of the longitudinal wave (was observed in two experiments only), velocity  $c_{obs}$  of the observed wave (which is very likely a surface wave, see section 7.2, p.76), velocity  $v_c$  of single cracks and their number  $C$  (an  $f$  in this column means that no single cracks but rather a crack field were found), velocity  $v_f$  of a crack field if there was one, picture separation time (framing rate)  $f-r$ , and remarks.

A total of 16 experiments with alumina tiles has been performed. With four experiments the trigger did not work. This gave rise for efforts to improve the trigger design which have been mentioned earlier in section 3.2. One experiment, # 999, was designed to measure the pressure in the wave. The target in this case was not polished and evaporated and the photographic method not applied. It turned out, however, that the performance of this measurements would have required a separate series of experiments and was, therefore, omitted. The photographs of shot # 5560 could not be evaluated because all pictures were overexposed by bright light generated by the impact event. Consequently, in these six experiments no optical data could be collected.

The successful main experiments carried out with alumina

shot #	$v_p$ m/s	$z_o$ m	$c_L$ mm/ $\mu$ s	$c_{obs}$ mm/ $\mu$ s	$v_c$ mm/ $\mu$ s	C	$v_f$ mm/ $\mu$ s	f-r $\mu$ s	remarks
999	181	-	-	-	-	-	-	-	un-coated
998	182	0.5	-	5.3	3.1	3-4	-	1	
997	239	0.14	-	5.8	3.4	1	-	1	
5556	519	0.75	-	5.7	4.6	4-6	-	2	
5555	611	0.75	-	-	-	-	-	2	trigger failure
5567	687	0	-	-	4.7	8	-	2	
5554	774	0.75	-	5.4	4.9	6	-	2	
5553	790	0.75	-	-	-	-	-	2	trigger failure
5558	1210	0.75	-	5.6	5.3	9	-	2	

Table 4 Test data; pointed projectiles

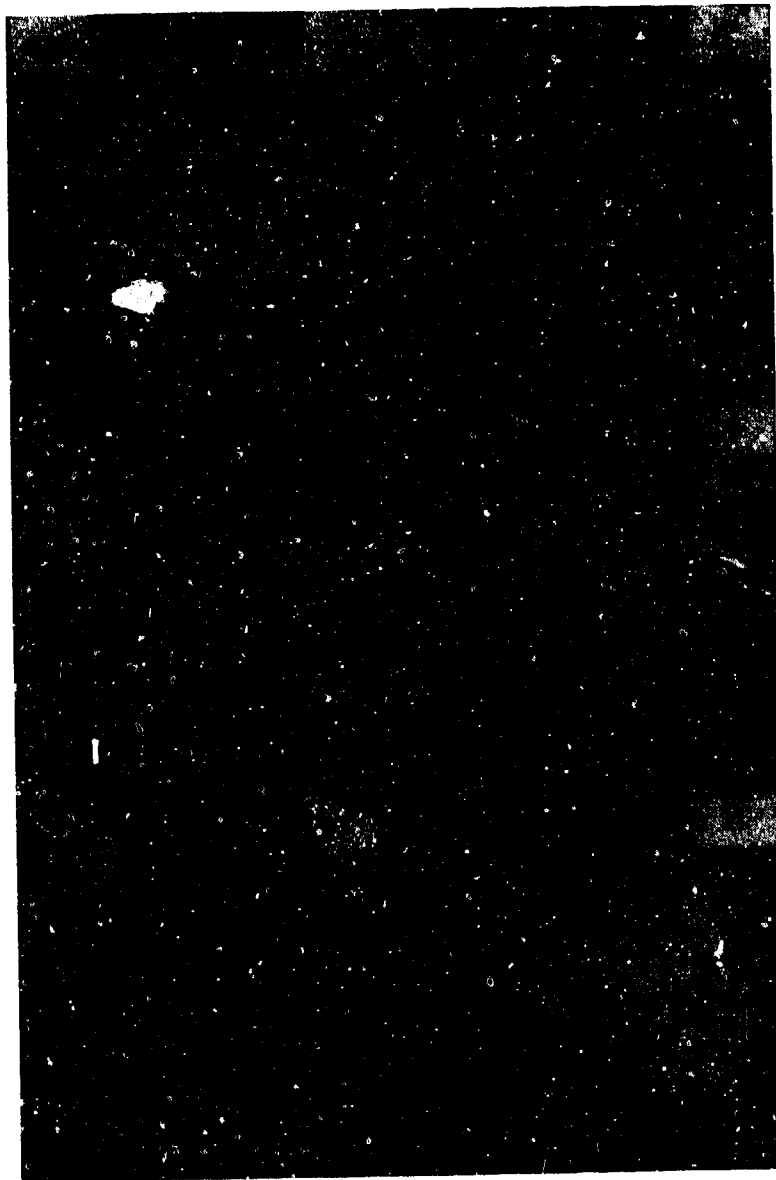
shot #	$v_p$ m/s	$z_o$ m	$c_L$ mm/ $\mu$ s	$c_{obs}$ mm/ $\mu$ s	$v_c$ mm/ $\mu$ s	C	$v_f$ mm/ $\mu$ s	f-r $\mu$ s	remarks
1000	101	0.5	-	5.4	5.2	5	-	1	
995	195	0.14	-	-	-	-	-	1	trigger failure
996	194	0.14	10.2	-	-	6-13	8.3	1	trigger failure
5561	557	0.75	-	-	-	-	-	2	trigger failure
5570	707	0.75	-	-	-	f	8.5	2	
5542	1062	0.75	10.47	-	-	f	9.5	2	
5560	1483	0.75	-	-	-	-	-	2	impact flash

Table 5 Test data; blunt projectiles

tiles of the size 100 mm \* 100 mm \* 10 mm are described in the following. Each shot is represented by the six most interesting high speed photographs out of the available 24 pictures. These are supplemented by a space-time diagram of moving events taken from the pictures, i.e. of waves and cracks. In these diagrams the time axis is given in terms of microseconds. The space axis is usually representing the direction of projectile propagation, however, can also mean the propagation direction of a moving crack tip (see for example # 998 with curved crack propagation), in order to determine its speed.

In all diagrams the longitudinal wave front ( $c_L = 10.4\text{mm}/\mu\text{s}$ ) and the rarefaction wave reflected at the tile's rear edge are plotted. This triangle is considered to be one of the bordering frames outside of which the stress-strain situation is less easy to understand because of a complicated wave superposition situation, and effects appear to be more complex than inside.

Symbols are consistently used in all these diagrams: ( $\square$ ) characterizes the observed wave, ( $\times$ ) the crack tip positions and (\*) means the extension of the black area.



998

Fig.28 Alumina tile impacted by a pointed projectile  
(162 m/s);

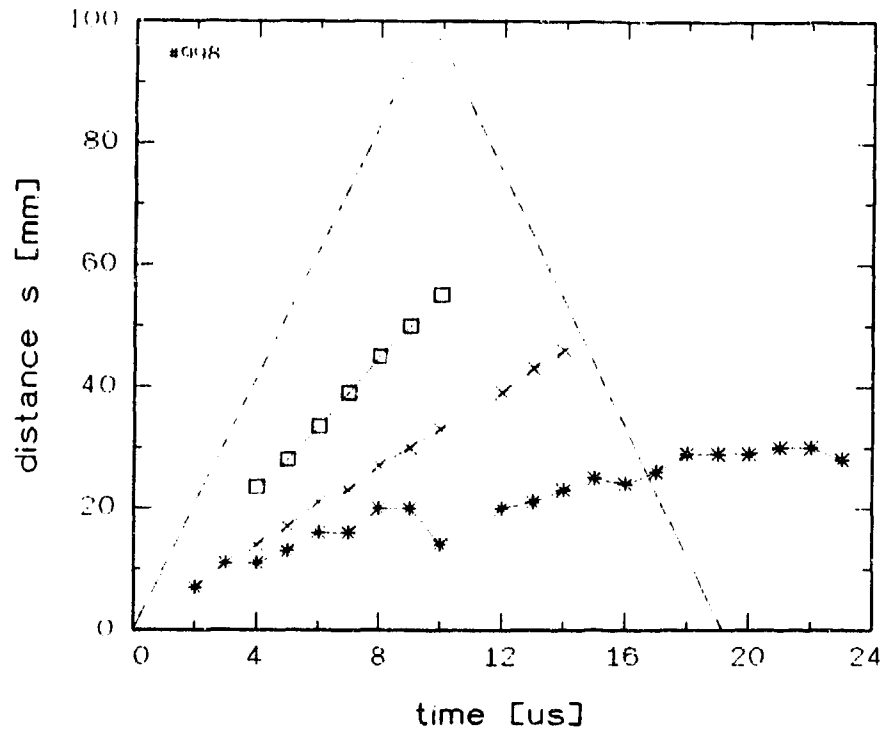


Fig.29 Space-time diagram of # 998

Description # 998

This experiment shows the development of a damage zone (black area, no details can be identified) at the impact site, an emanating wave and after  $4\mu\text{s}$  four cracks leaving the black area with a high velocity. These four cracks reduce to three ( $8\mu\text{s}$  after impact) and two ( $13\mu\text{s}$  after impact). In particular, one of these vanishing cracks can be observed during this process. It becomes thinner and finer and, obviously, closes. This crack does not grow anymore while this process takes place. The two outer cracks propagate, instead, on a circular path to form a shape like a crab's claw. The crack path is rough and fuzzy

and there is a furcation tendency which leads to the assumption that these cracks propagate with their terminal velocity. Both cracks form a claw-like curvature by developing the inner branches at the expense of the outer ones. This is the process when the large central part of the target which can be seen in Fig.48a (recovered target, p.67) is cut out. Two additional bright cracks appear at about  $16\mu\text{s}$  after impact. They do not originate from the two expanding cracks or from the black area, but rather occur like spall fractures. Although they grow somewhat with time, their speed is rather modest (see Fig.29).

The black area at the impact site remains mysterious in most of the experiments. It is assumed that with high impact velocities the material there is destroyed into very fine debris. In some cases, however, for which this experiment is an example, parts of the black area become visible again for some time and show some details of the surface. From this is concluded, that still larger parts within the black area remain undestroyed and are tilted only to reflect the light in another direction.



997

Fig.30 Alumina tile impacted by a pointed projectile  
(239 m/s);

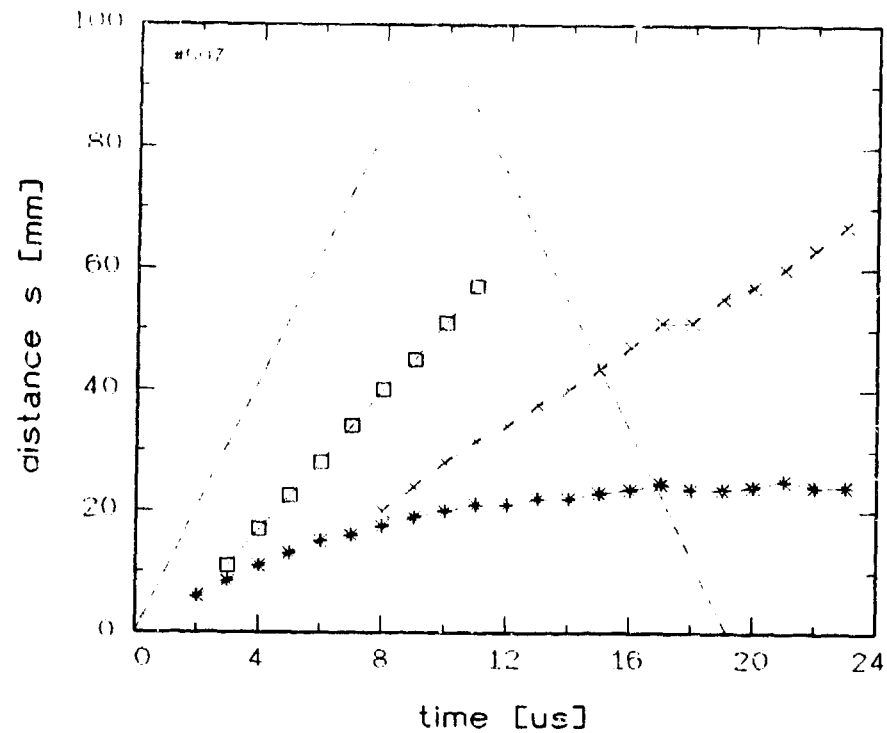
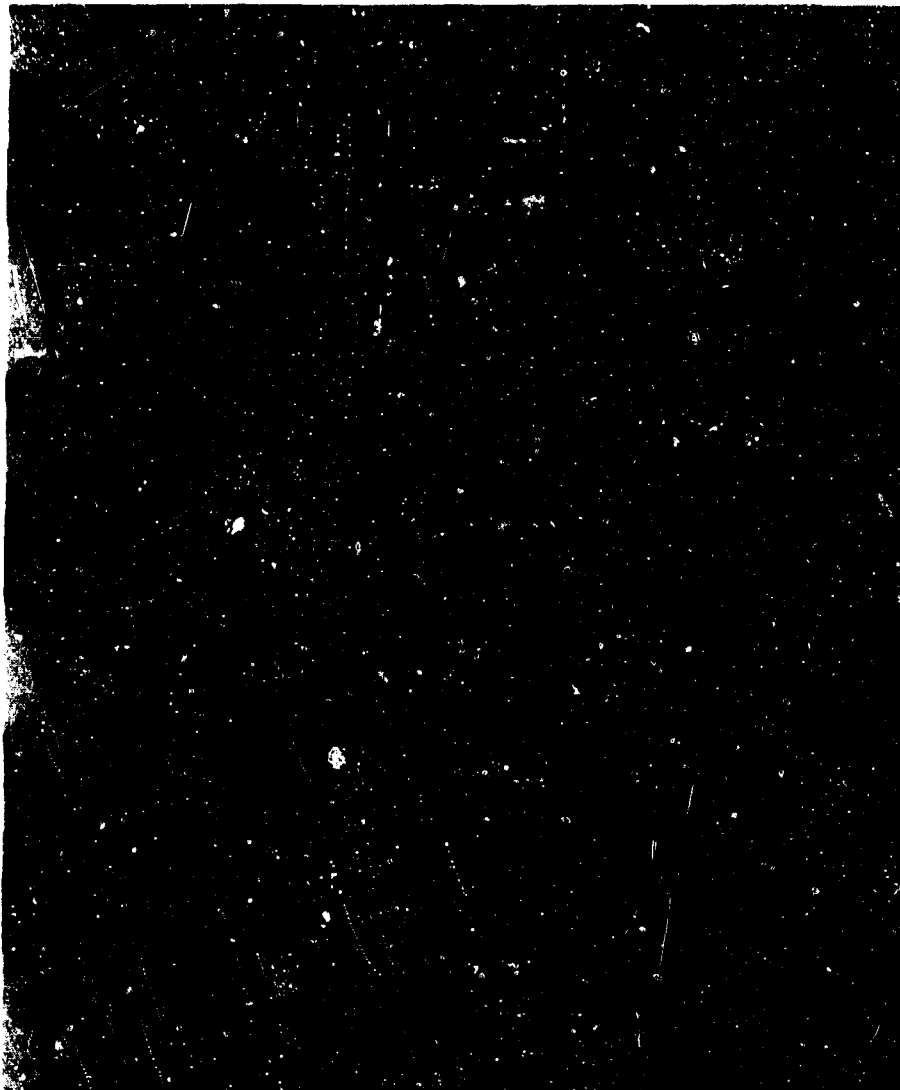


Fig.31 Space-time diagram of # 997

Description # 997

The impact conditions were the same as in the experiment before, only the impact velocity was higher. The fracture appearance photographed by the high speed camera is quite different, though. The black area expands with a low velocity almost circularly. Only one crack has been produced which leaves the black area. Again, this one propagates very fast, it becomes rough and bifurcates. However, there is not a strong tendency to develop a curved crack propagation as it was before.



5556

Fig.32 Alumina tile impacted by a pointed projectile  
(519 m/s);

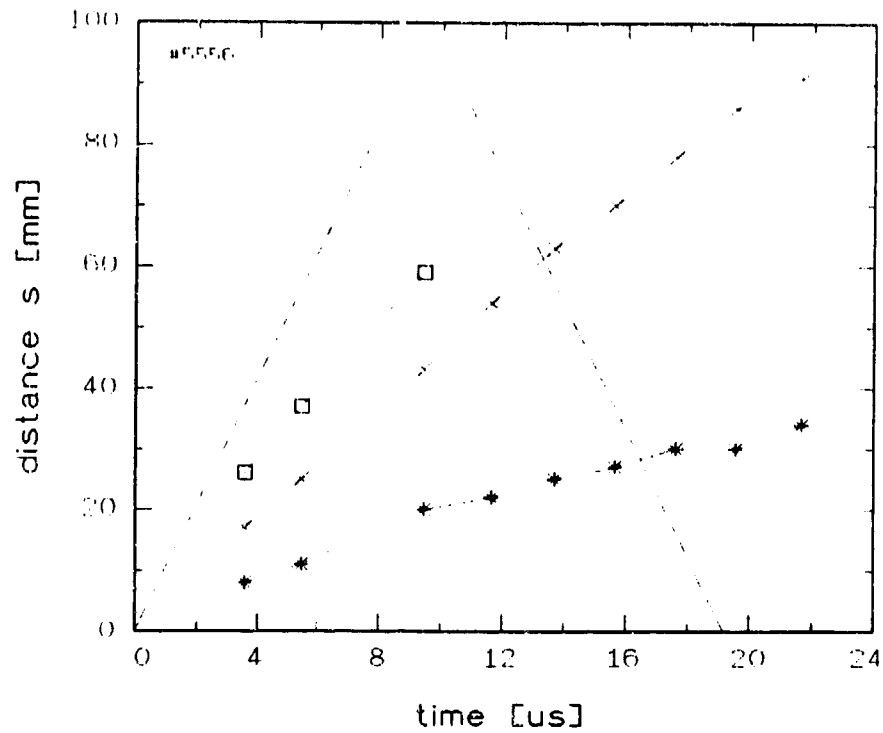


Fig.33 Space-time diagram of # 5556

Description # 5556

An extended and irregular shaped black area with parts of it bordered by running cracks leads to the assumption that only parts of the area may have been destroyed into fine debris. Those parts being bordered by cracks may still be intact fragments and appear black by tilt or bending.

Three cracks can be seen very early. The number of cracks increases after some time by bifurcation.

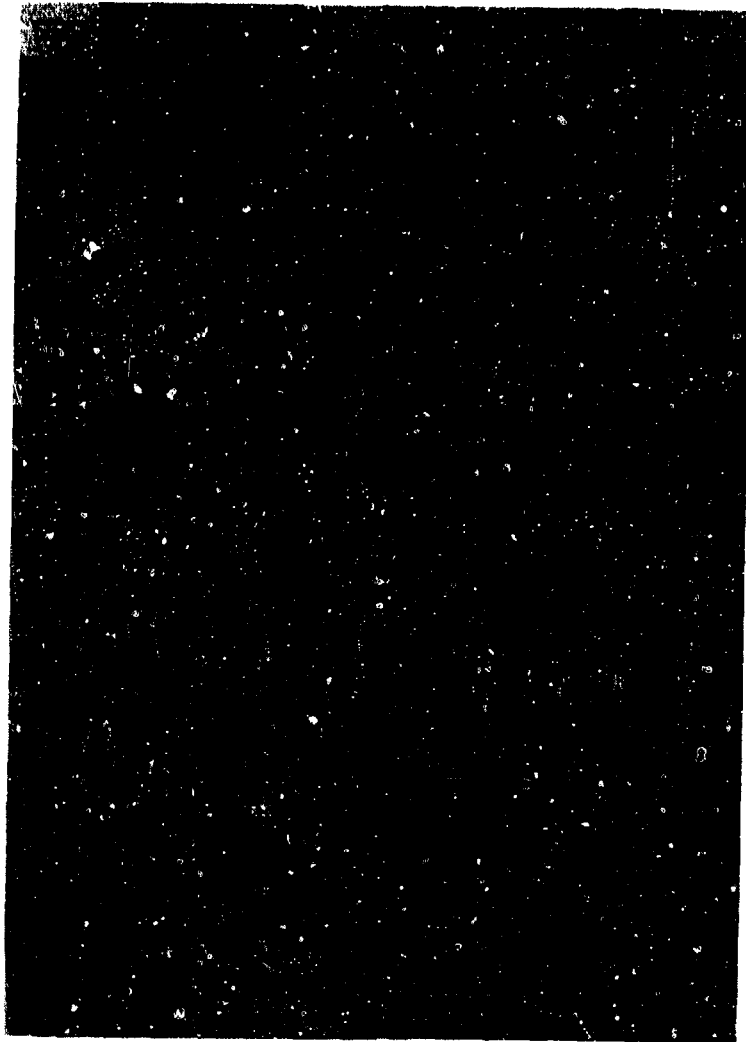


Fig.34 Alumina tile impacted by a pointed projectile  
(687 m/s);

5367

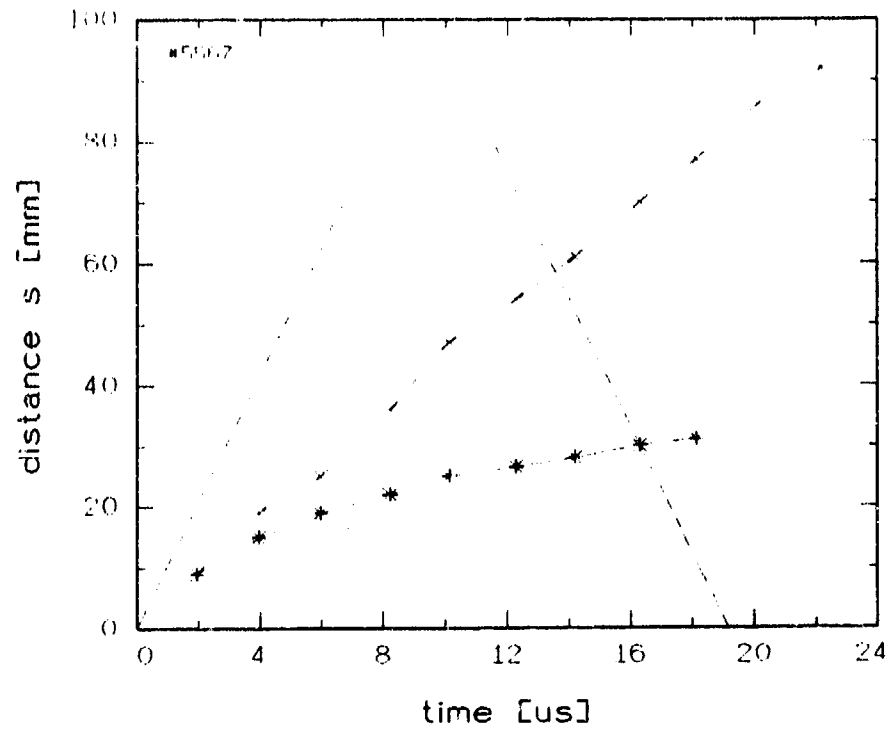


Fig.35 Space-time diagram of # 5567

Description # 5567

This experiment exhibits a slightly increased number of cracks due to the faster impact velocity. The camera was focused onto the target surface, waves cannot be seen anymore, therefore. Bright glowing particles, perhaps from the steel bullet, were moving all over the picture area illuminating all 24 lenses at the same time. The shape of the black area is again jaggy and large, dark fragments are bordered by moving cracks.



5554

Fig.36 Alumina tile impacted by a pointed projectile  
(774 m/s);

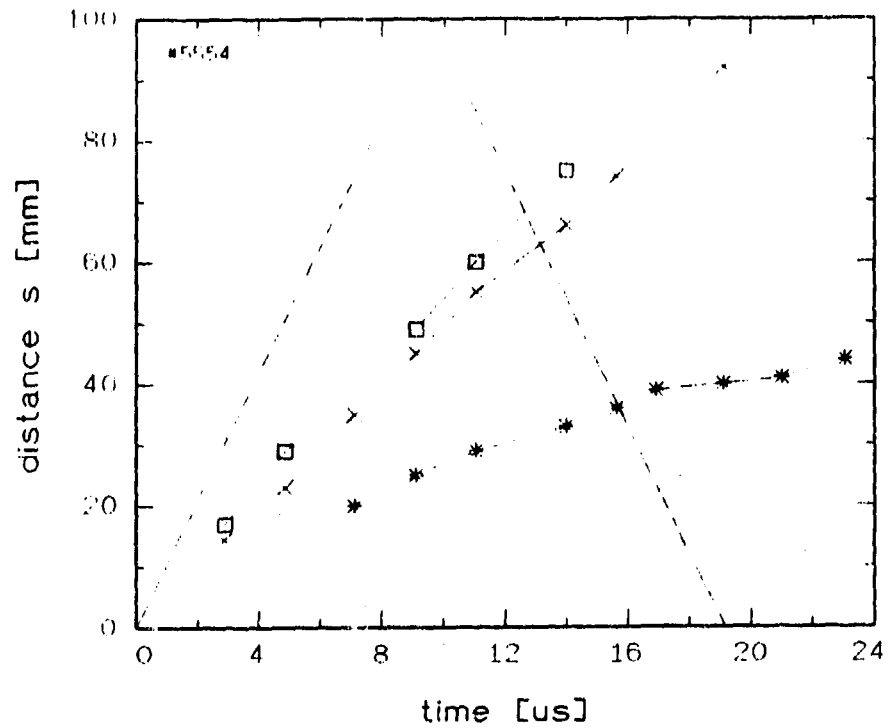


Fig.37 Space-time diagram of # 5554

Description # 5554

This experiment is very similar to the previous one. The reference plane distance  $z_0 = 0.75$  m makes waves visible again. A central part of the black area is of particular interest (see picture at  $22.5 \mu\text{s}$  after impact). This part being black up to about  $20 \mu\text{s}$  after impact becomes visible again. The traces of two of the cracks can be seen within this part. However, the trace of a third crack is not visible, this means obviously that this one started outside this part, perhaps from a circumferential crack.



5558

Fig.38 Alumina tile impacted by a pointed projectile  
(1210 m/s);

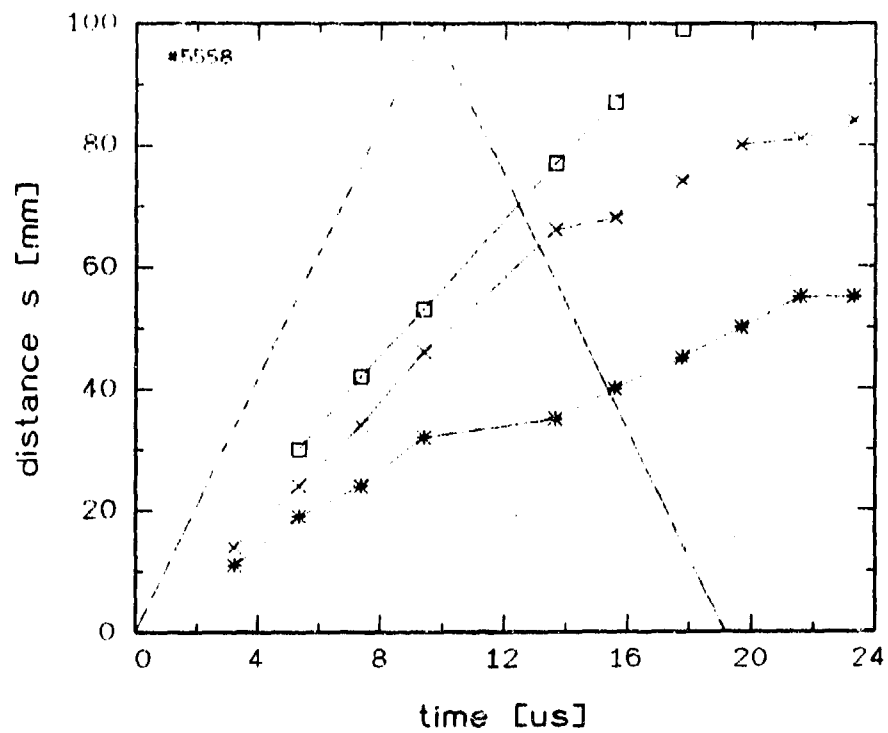


Fig.39 Space-time diagram of # 5558

Description # 5558

Within a few microseconds shortly after the impact event the appearance of the expanding cracks of this test is very similar to those of glass experiments. The front of the crack tips seems to be circular and suggests a common terminal crack velocity. Later on a part of this front separates from the crack tips and is identified to be a wave preceding the cracks.



1000

Fig.40 Alumina tile impacted by a blunt projectile  
(101 m/s);

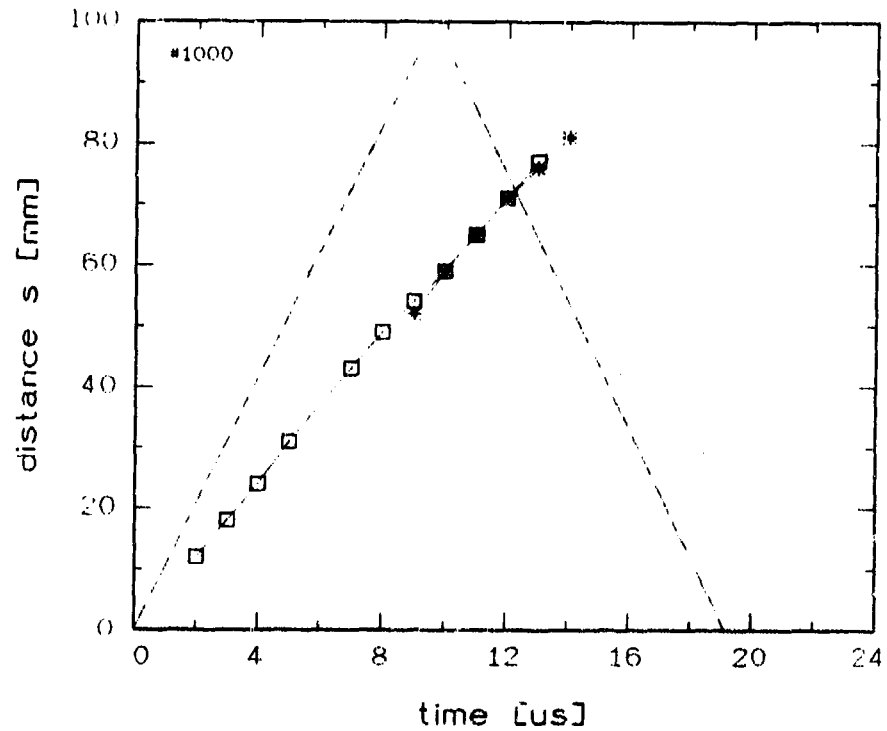


Fig.41 Space-time diagram of # 1000

Description # 1000

The number of generated cracks seems to increase by bifurcation during the damage developing phase. This experiment also gives hints that crack nucleation may occur ahead of the original crack tips.

Waves are generated at the two edges of the blunt projectile (diam. 49 mm). Obviously, the collision was not very accurate. The contact at the upper edge occurred about  $0.75 \mu\text{s}$  earlier than the one at the lower edge (this corresponds to a tilt of about  $75 \mu\text{m}$  with that impact velocity). This follows from the different propagation distances of the two waves.



Fig.42 Alumina tile impacted by a blunt projectile  
(194 m/s);

996

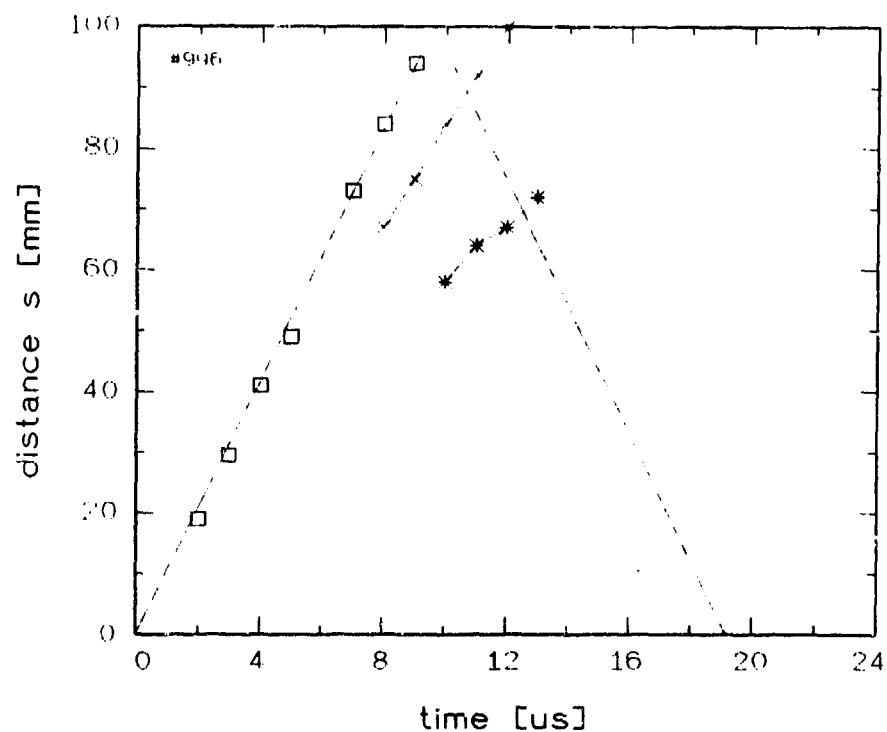
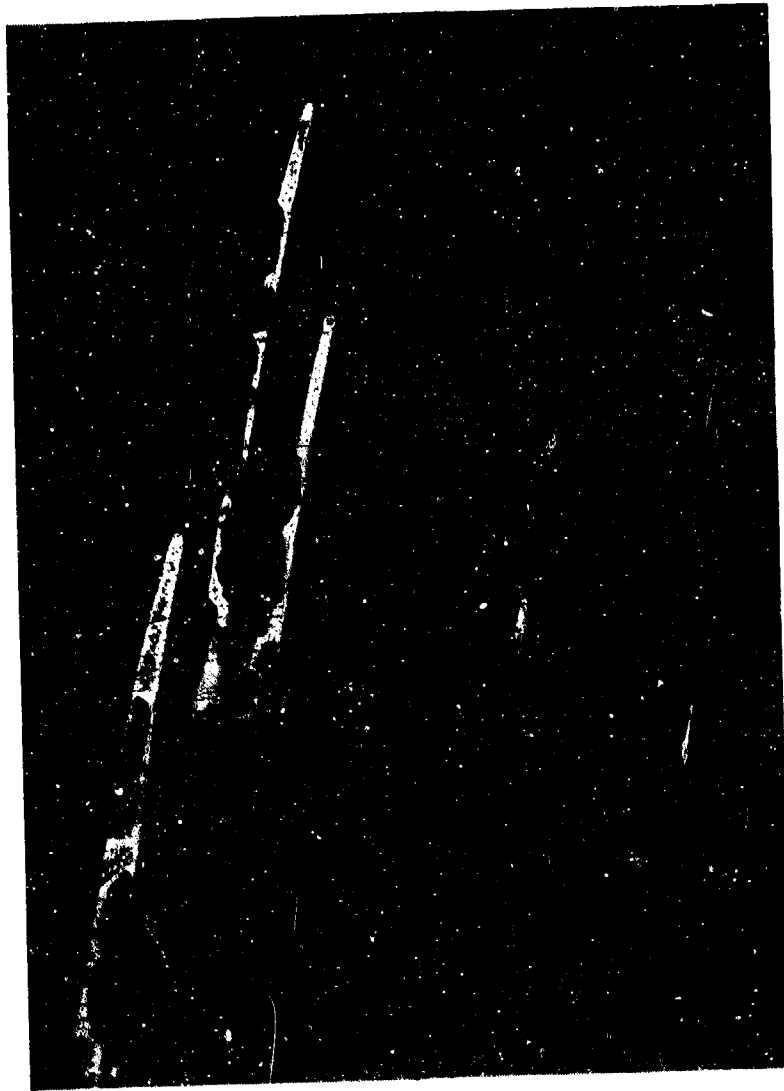


Fig.43 Space-time diagram of # 996

Description # 996

With this experiment the collision area was also a large one (diam. 49 mm). Due to the higher impact velocity the damage events in the target are much more complicated than before. Striped patterns which move with almost longitudinal wave speed may be caused by fractured material right behind the first wave front. Later on the well-defined border of a crack field develops with a very high speed. Single cracks cannot be resolved anymore.

Bright patterns occur in front of even the longitudinal wave front. Light of an unknown source seems to be reflected into the camera.



5570

Fig.44 Alumina tile impacted by a blunt projectile  
(707 m/s);

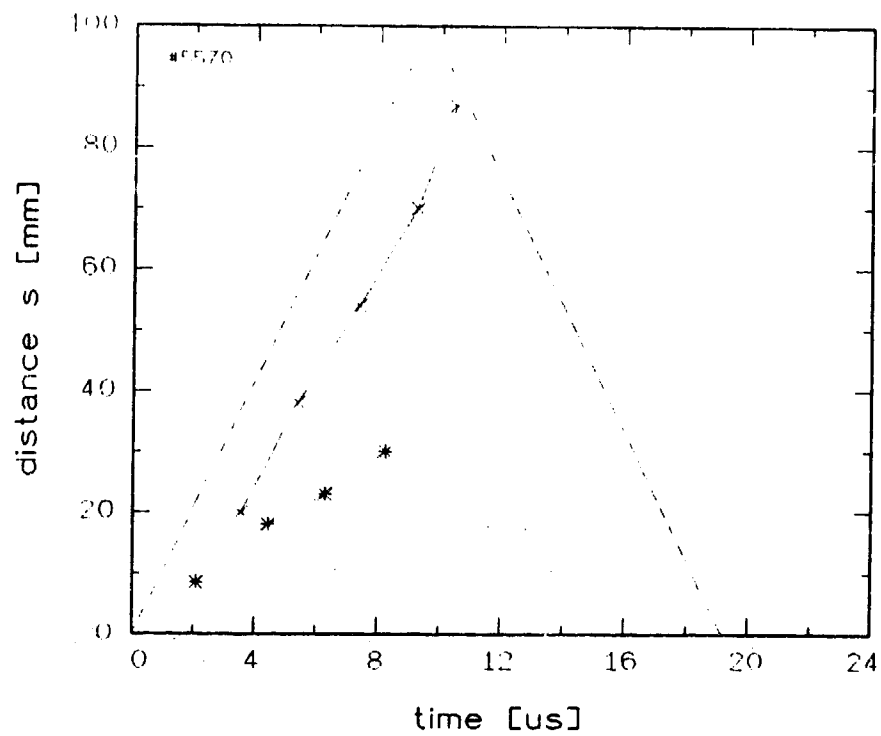
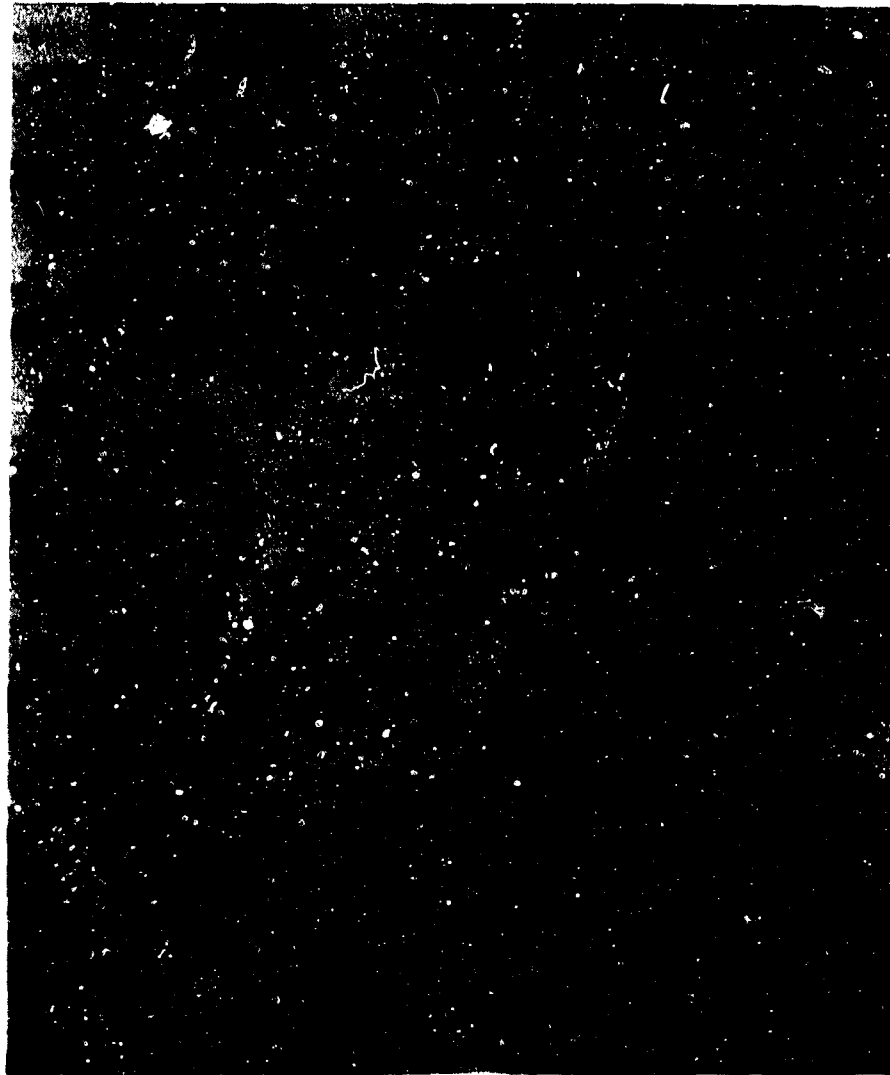


Fig.45 Space-time diagram of # 5570

Description # 5570

This experiment (contact area 13mm \* 10mm) shows the two fields, the fast expanding black area with irregular parts and the well-defined crack field which expands almost circular but less exactly as a crack field in glass would do (see Fig.21, for example).



5542

Fig.48 Alumina tile impacted by a blunt projectile  
(1062 m/s);

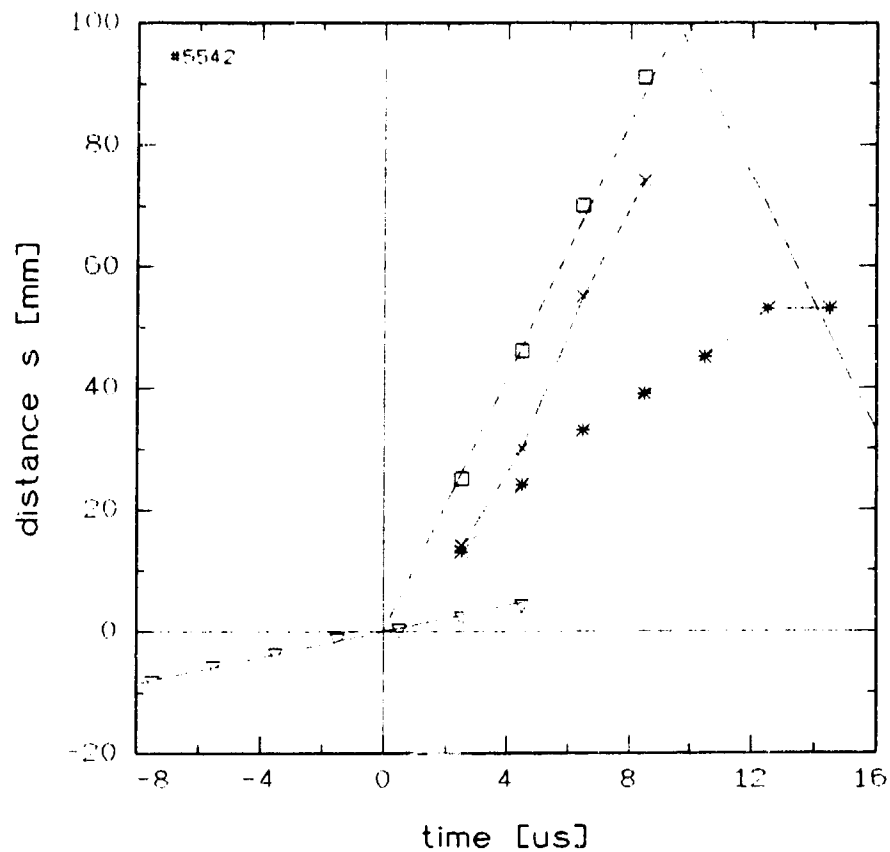


Fig.47 Space-time diagram of # 5542

Description # 5542

This experiment differs considerably from all previous ones. The wave which can be observed is obviously the longitudinal wave front. Also the crack system appears to propagate faster than others before, with only little less than the longitudinal wave speed. Even the black area exhibits a very high speed. Some pictures at the beginning show the movement of the projectile prior to the impact, this has been drawn also in the diagram of Fig.47.

## 6.2 Target Recovery

It has been mentioned before (section 6.1) that most fragments of target # 998 could be recovered and put together. A photograph of this re-assembled target is shown in Fig.48a and, for comparison, also one of the pictures of the high speed series, # 24, has been added in Fig.48b. In this figure the fracture situation in the 23<sup>rd</sup> microsecond after impact is shown (picture #1 equals time zero). Obviously, this fracture occurrence demonstrates the process when the central part of the target was cut out by the "crabs claw"-shaped cracks. Fig.48b shows the cracks being fuzzy and it was expected to see rough fracture surfaces at this central piece. The inspection, however, did not reveal this. The crack surfaces are smooth like all the others and it must be concluded that many tiny side cracks were produced which arrested soon and then closed again.

Most of the fragments are large and could be positioned at their origin. This is different with those parts which originate from the impact region. These are small and even if they were found re-assembling was not possible. It would, on the other hand, be of interest to recover just those parts of the target which could show the initiating fracture situation. This happened, fortunately, in one experiment, # 995 (one of those with a failing trigger).

The experiments # 995, # 996, and # 1000 were loaded by Armco iron flyer plates. 49 mm diameter and 10 mm thick. All of these flyer plates are recovered and show an indentation at the impact site. This is a small slot with a depth of 1 mm with the # 1000 target ( $v_p = 101$  m/s). The two others, # 995 and # 996, show bigger slots, 3 mm deep,

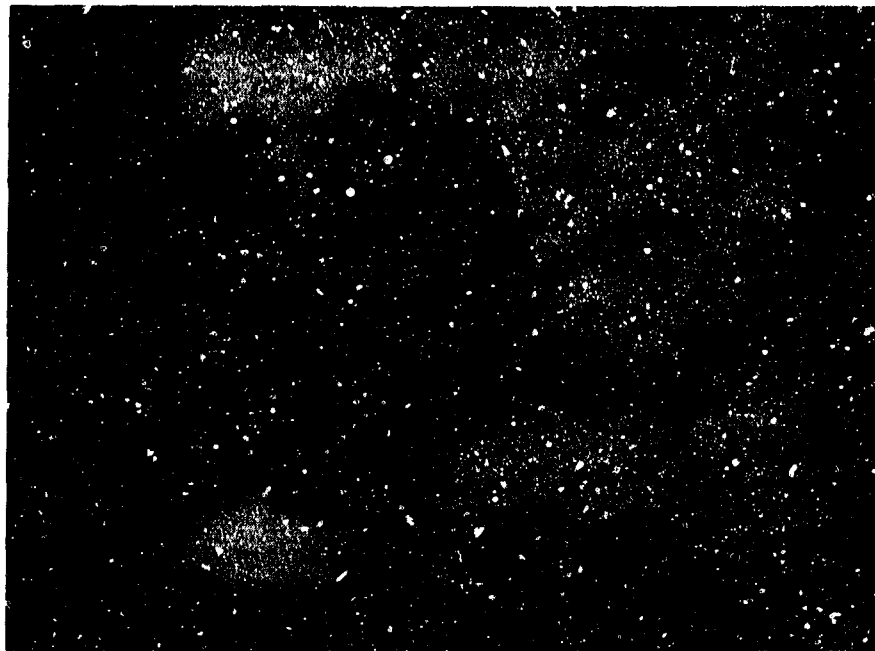


Fig.48a Recovered and re-assembled target of # 998

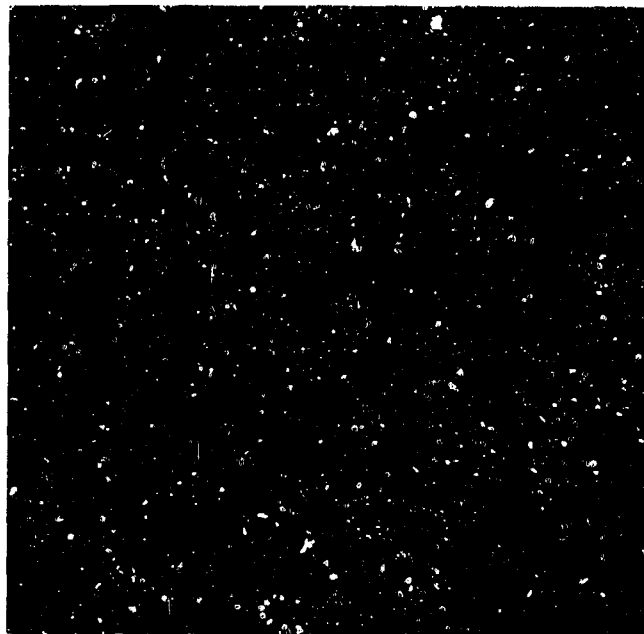


Fig.48b Picture # 24 of the high speed series of # 998

( $v_p = 195$  m/s, for the data see Table 5). Soon after impact bending of the flyer plate occurs with the result that parts of the breaking target at the impact site are fixed to the iron plate by clamping. This is schematically demonstrated in Fig.49a and b. With the flyer plate # 1000 an unbroken larger part of the target remained in the slot. The plate of # 996 broke in two parts and shows the indentation very nicely but no target parts were recovered. Of most interest is # 995. Pictures of this plate are shown in the following.

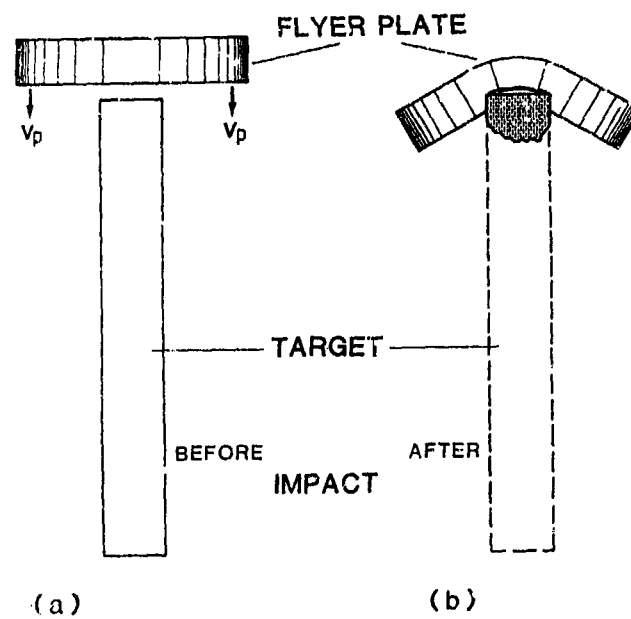


Fig.49 Scheme of flyer plate experiment and clamped target fragments

Figs.50 and 51 show this recovered flyer plate in front and up-side view. An enlargement of the front view is shown in Fig.52 (already gold sputtered for the SEM) and a detail of the fragmented ceramic in Fig.53. Scanning electron microscope (SEM) pictures of the visible ceramic surface (details of Fig.52) are presented in Figs.54 and 55.

The mechanism leading to this phenomenon seems to be as follows. The ceramic material being much harder than the iron penetrates the plate with decreasing velocity and finally stops. Even if this would happen with constant velocity and subsequent sudden arrest this penetration process would last  $15 \mu s$  ( $v_p = 200 \mu m/\mu s$ ). Within this time the initially produced fracture has completely developed. When the middle part of the flyer plate reduces velocity inertia causes the outer parts to further move and bend the plate this way. This is the clamping process. Friction and bending of the plate is also the reason for a shear loading of the ceramic material at the contact area since the outer parts of the slot move faster than the inner ones. It was observed ( $\times 1000$ ) that the centre of the slot can even move backwards and loose contact. This shear loading seems to be responsible for a laminated or slaty fracturing of the ceramic material as is shown in the figures (e.g. Fig.53). The thickness of the layers ranges between 0.1 and 1 mm.

The micrographs with the lower magnification (Fig.54) show coarse and fine fragmented material, fragments from the shear loading. The micrographs with the larger magnification, Fig.55, show details of the loading. The upper picture shows unbroken grains which may be an opened

imperfection of the material but may also result from a low velocity fracture event. The middle one shows a very flat crack surface with cleaved grains which could be generated by a fast crack propagation. A spall-like sudden rise of stress in a narrow distribution of high magnitude could also be the reason of this phenomenon. Even more complicated is the fracture configuration shown in the lower picture. This exhibits a cube corner formed by three flat surfaces showing grain cleavage, too.

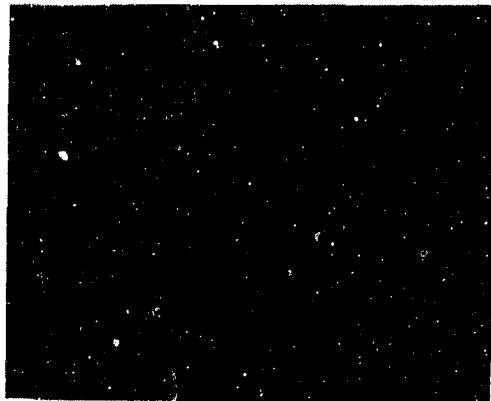


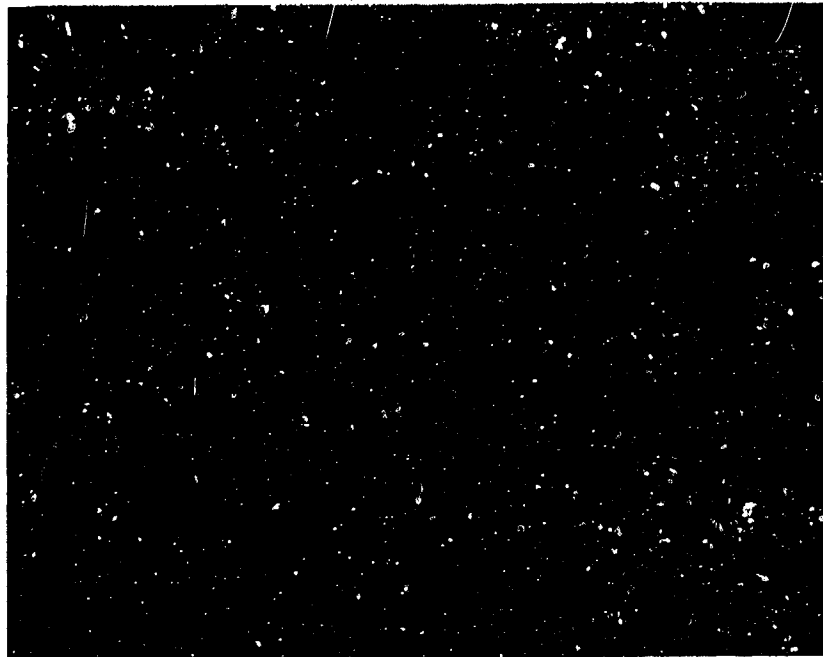
Fig.50 Recovered flyer plate # 995, Armco iron, 49 mm diameter, 10 mm thickness, front view



Fig.51 Recovered flyer plate # 995, Armco iron, 49 mm diameter, 10 mm thick, enlarged up-side view



Fig.52 Recovered flyer plate # 965, Armco iron, 49 mm diameter, 10 mm thick, enlarged front view



| ←                      10 mm                      → |  
(= thickness of the target)

Fig.53 Recovered flyer plate # 995, Armco iron, 49 mm diameter, 10 mm thick, detail of Fig.52

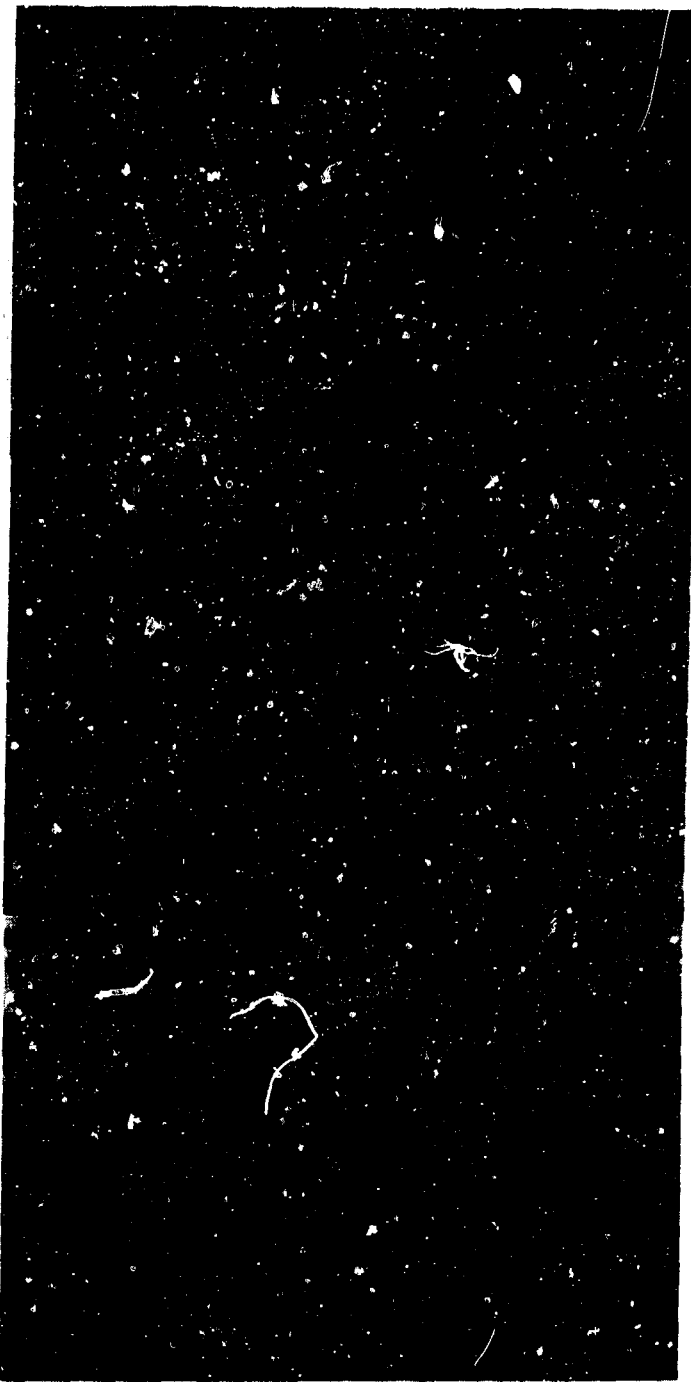


Fig.54 SEM micrographs of fractured alumina (from Fig.52)

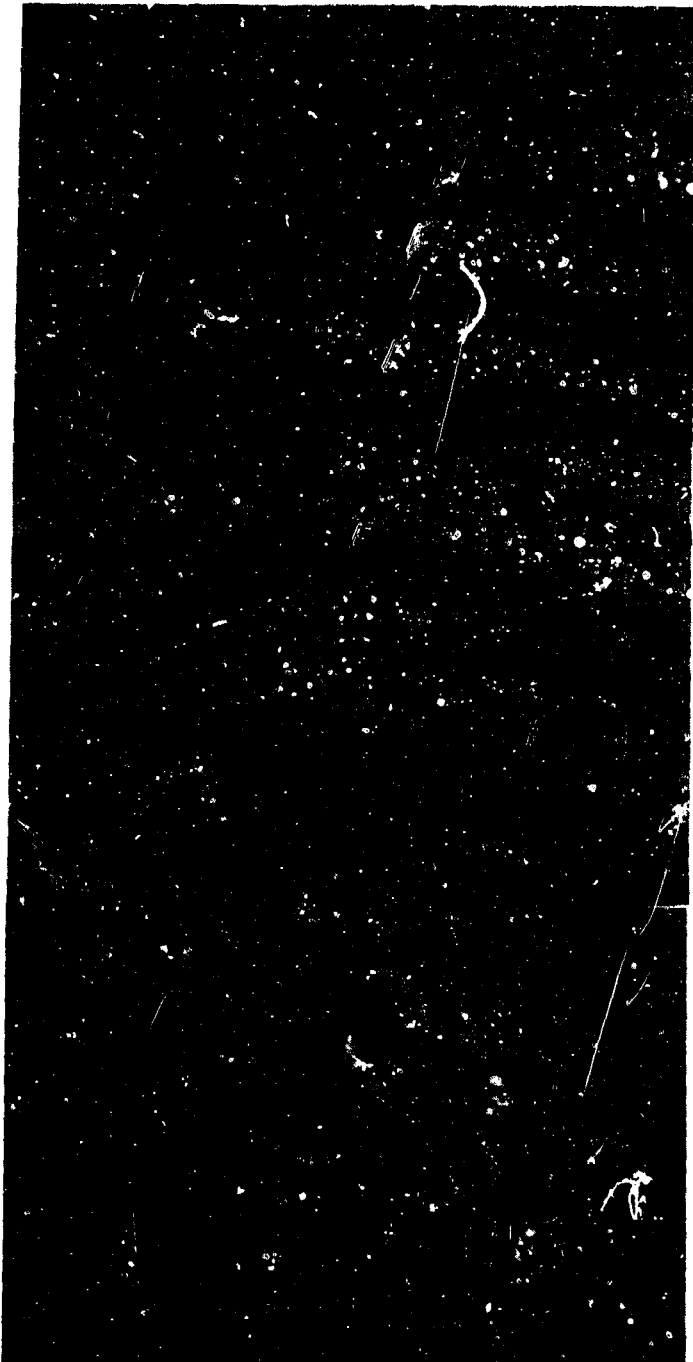


Fig.55 SEM micrographs of fractured alumina (from Fig.52)

## 7. ANALYSIS OF WAVE AND FRACTURE PHENOMENA

### 7.1 Evaluation of Wave Data

In some of the experiments waves can be seen on the photographs. The velocities of these waves (and also of the cracks) were determined by measuring the wave and crack tip positions on the pictures (the picture number is correlated to time). All velocity data evaluated from the pictures (given also in Tables 4 and 5, Chapter 6) are calculated step by step from the change of the positions on the pictures,  $\Delta s$ , and the time difference,  $\Delta t$ , between subsequent pictures:  $v_i = \Delta s_i / \Delta t_i$ . From these the average

#	$c_{obs}$ (mm/ $\mu$ s)		$c_{crack}$ (mm/ $\mu$ s)	
	long.	trans./surf.	single	field
938	-	5.3 $\pm$ 0.5	3.1 $\pm$ 0.6	-
997	-	5.8 $\pm$ 0.4	3.4 $\pm$ 0.6	-
5556	-	5.7 $\pm$ 0.	4.6 $\pm$ 0.5	-
5567	-	-	4.7 $\pm$ 0.5	-
5554	-	5.4 $\pm$ 0.4	4.9 $\pm$ 0.5	-
5558	-	5.6 $\pm$ 0.4	5.3 $\pm$ 0.6	-
1000	-	5.4 $\pm$ 0.5	5.2 $\pm$ 0.8	-
996	10.2 $\pm$ 0.8	-	-	8.3 $\pm$ 0.5
5570	-	-	-	8.5 $\pm$ 0.8
5542	10.47 $\pm$ 0.06	-	-	9.5 $\pm$ 1.4

$\bar{c} = 5.5 \text{ mm}/\mu\text{s}$

Table 6 Observed velocities

value was calculated and the standard deviation is determined. These data are listed in Table 6. This scatter is due to the small number of individual data and the limited accuracy of the position reading. Table 6 also shows the crack velocity data which are analysed in Section 7.2.

In shot # 5542 the velocity of the wave is determined to be 10.47mm/μs. This is almost accurately the previously [8] determined longitudinal wave speed ( $c_L = 10.44\text{mm}/\mu\text{s}$ ). With this exception the velocities of all the waves were found to be in the range of 5.3 to 5.8mm/μs with a calculated mean value of 5.5 mm/μs. This is about one half of the longitudinal wave speed. It is, therefore, to expect that this wave represents either the transverse (shear) wave or a surface (Rayleigh) wave.

This can be decided using the wellknown relations (see for example [9]) between the wave speeds  $c$  and the Poisson's ratio  $\nu$  for an isotropic elastic body:

$$\frac{c_R}{c_T} = \frac{0.87 + 1.12\nu}{1 + \nu}, \quad (3)$$

$$\frac{c_T}{c_L} = \sqrt{\frac{1 - 2\nu}{2(1 - \nu)}}, \quad (4)$$

$$\frac{c_R}{c_L} = \frac{c_T}{c_L} * \frac{c_R}{c_T}, \quad (5)$$

with the indices R, T, and L synonymously for Rayleigh, transverse, and longitudinal wave, respectively. These equations are plotted in Figs.56a and b.

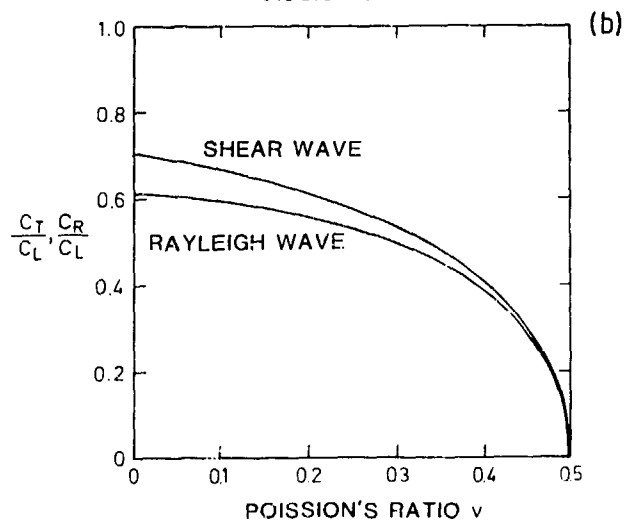
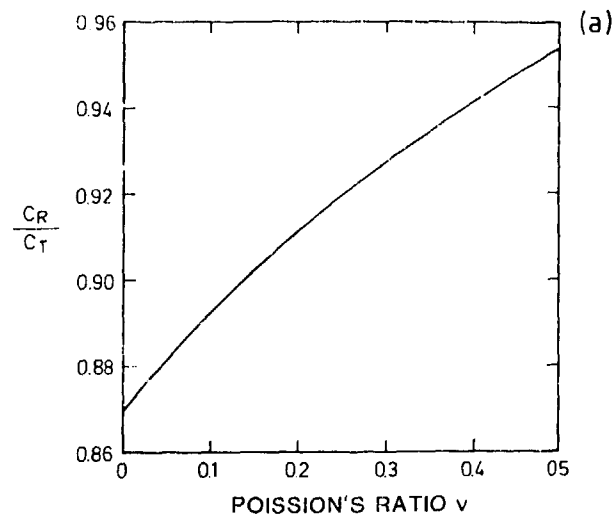


Fig.56 Correlations between wave velocities and Poisson's ratio (eqs. (3) to (5))

In Table 7 Poisson's ratios are computed for the observed wave velocities,  $c_{obs}$ , with the aid of eqs.3 to 5 or Fig.49. The abbreviations T and R in rows 3 and 4 indicate that the Poisson's ratios given in these rows are computed with the assumption of the observed wave being either a transverse (T) or a Rayleigh (R) wave.

$c_{obs}, \frac{mm}{\mu s}$	5.3	5.4	5.5	5.6	5.7	5.8
$c_{obs}/c_L$	0.5077	0.5172	0.5268	0.5364	0.5460	0.5556
T, $\nu =$	0.3264	0.3174	0.3079	0.2980	0.2876	0.2767
R, $\nu =$	0.2847	0.2714	0.2570	0.2413	0.2242	0.2056

Table 7 Evaluation of the observed waves

The results can be discussed in two different ways:

1. From data sheets it is known that the Poisson's ratio of alumina does not vary very much and has the magnitude

$$\nu = 0.22.$$

If this is assumed to be true it follows from Table 7 with  $\nu = 0.2242$  that the observed waves are Rayleigh waves and exhibit a speed of about

$$c_R = 5.7 \text{ mm}/\mu s.$$

With eq.(3) the corresponding shear wave velocity is calculated to be

$$c_T = 6.2 \text{ mm}/\mu s.$$

2. With the average value of the wave velocity calculated in Table 6,

$$\bar{c}_{\text{obs}} = 5.5 \text{ mm}/\mu\text{s}$$

a Poisson's ratio of either

$$\nu = 0.3079 \quad \text{or} \quad \nu = 0.2570$$

is computed (third column in Table 7) depending on the observed wave being either a transverse or a surface (Rayleigh) wave, respectively. With the assumption that the lower value is the more likely one (since it fits better to the value  $\nu = 0.22$  given in data sheets, and the upper value, being almost 0.31, seems to be unrealistic high for this material) it is again concluded that the observed wave is a surface wave,

$$c_{\text{obs}} = c_{\text{R}} = 5.5 \text{ mm}/\mu\text{s}.$$

From this follows

$$c_{\text{T}} = 5.9 \text{ mm}/\mu\text{s}$$

being the corresponding velocity of the transverse wave.

This conclusion, the observed waves being Rayleigh waves, is supported by the fact that surface waves deform the reflecting surface and, consequently, deflect light much more than longitudinal or even transverse waves would do. This is well known from shadow optical investigations with steel.

The wave velocity data given in Table 6 are plotted in Fig.57 versus the impact velocity. The velocities of both waves, the average value of Table 6 (5.5 mm/ $\mu$ s) and the Rayleigh wave based on  $\nu = 0.22$  (5.7 mm/ $\mu$ s), fit into the wide scatter band. For a decision which of the two values is closer to the correct one the number of data points is insufficiently small. An assumed dependence of material

parameters ( $\nu$ ,  $E$ , ...) on the dynamic loading conditions which would cause a tendency of the wave velocities cannot be seen.

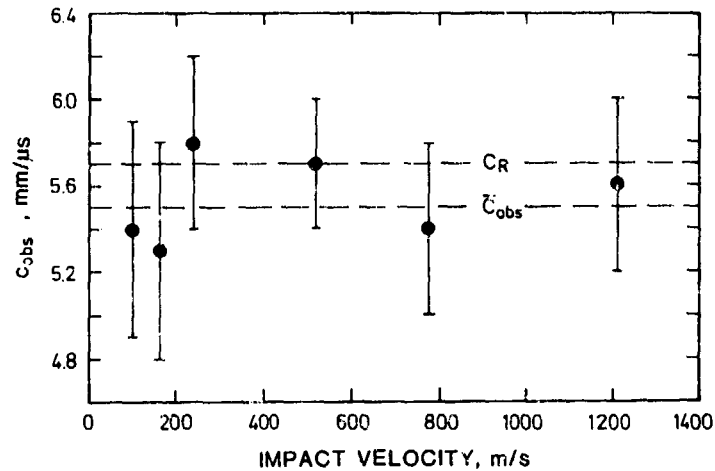


Fig.57 Velocity of the observed waves vs. impact velocity

## 7.2 Evaluation of Crack Data

### 7.2.1 Crack velocities

Attention must be focused onto the black area. The material at the impact site is assumed to be at least in parts comminuted into fine debris with particle sizes between 1 and 10  $\mu\text{m}$ . A rough estimation (the total amount of the debris volume and the  $\bar{x}_{50}$ -value remained unknown) resulted in a fracture area of the order of at least  $10^4 \text{ cm}^2$ . For a crack which separates the target into two pieces, on the other hand, an area of the order of  $10 \text{ cm}^2$  has to be generated. The energy required to produce the single crack is probably in the per cent region of that of

the debris. From this follows that most of the input energy is consumed for particle comminution and only a tiny fraction remains for macroscopic fracturing processes.

This consideration should consequently be one guideline for future investigations of energy absorption effects with brittle behaving material like glass and ceramics. The debris should be recovered and carefully analysed utilizing the methods of particle comminution. This would lead to results which possibly can explain details of the absorption processes.

The evaluation of macroscopic fracture events photographed with the high speed camera, nevertheless, leads also to interesting results. The crack velocities given in Table 6 are determined in the same way as the wave velocities. Again the standard deviations show mainly the uncertainty of the position determination on the pictures. These data are plotted in Fig.58 versus the impact velocity, and from these curves it becomes evident that a terminal crack velocity below any wave velocity does not exist. The crack speed depends on the loading conditions. It increases with increasing impact velocity. This is a new and surprising finding of this work.

Fracture mechanics states that under uniaxial loading conditions the crack speed can vary only up to a certain limit. This "terminal crack velocity" was theoretically determined by, e.g., Yoffe [11], Broberg [12], and Freund [13] to be equal to the Rayleigh wave velocity:  $v_T = c_R$ . Experiments revealed this quantity to be of the order of

half the Rayleigh wave velocity:  $v_T \approx c_R / 2$ .

This has also been experienced with the glass experiments [3]. In no case a crack propagation speed was measured which exceeded the terminal velocity of  $\approx 1460\text{m/s}$  known for this glass. In the experiments with a pointed bullet impacting the glass target this is visualized by the locus of all crack tips forming a circle.

With the alumina experiments circles which indicate the same speed of the propagating cracks can also be seen in some experiments. The determined velocity was a constant, too, however, a different one from experiment to experiment, the magnitude obviously depending on the loading conditions (pointed or blunt projectile, impact velocity).

With the glass experiments always a large number of cracks were produced. This is also different with the alumina experiments. At low impact velocities only a few single cracks were generated. The number of cracks seems to increase with higher impact velocities. Crack fields as in the glass experiments were observed with very high impact velocities. Counting the number of cracks on the pictures was often quite difficult because of the crack appearance being not always very clear and the number of cracks not constant all the time. An attempt to collect these data in a diagram is made in Fig.59. In agreement with Fig.58 averaging lines are drawn that way that the assumptions of a constant and of an increasing number of cracks for certain regions of the impact velocity are met.

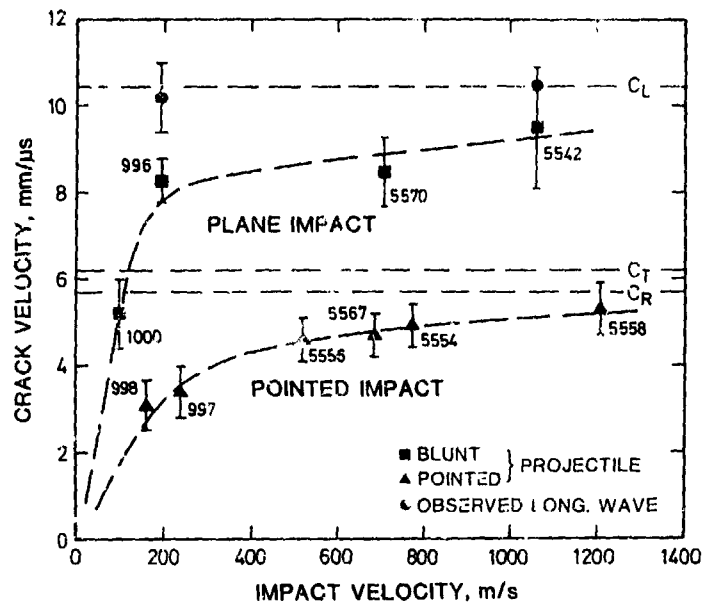


Fig.58 Crack velocity vs. impact velocity

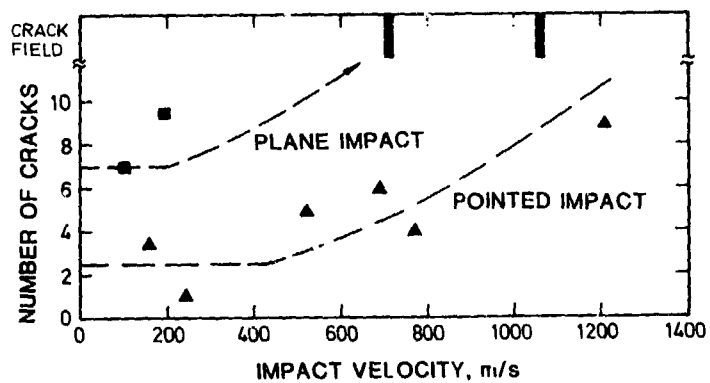


Fig.59 Number of cracks vs. impact velocity

Instead of considering the impact velocity (and according to eq.(2a) the generated pressure  $\sigma$ ) being responsible for the wave and fracture phenomena observed on the pictures it may be assumed that the energy transported by the shock wave or a certain fraction of it causes the damage of the target. In this case it would be more instructive to plot the data versus this energy. An approximate way to calculate the total wave energy is given in the following.

The energy density or specific energy (energy per unit volume) built up by a shock wave is given by

$$\delta = \frac{1}{2} \sigma_A \varepsilon + \frac{1}{2} \rho v_A^2, \quad (6)$$

with the first term being the potential and the second term being the kinetic part [10]. The compression  $\varepsilon$  can approximately be expressed by

$$\varepsilon = \frac{v_A}{c_L}, \quad (7)$$

and the state magnitudes  $\sigma_A$  and  $v_A$ , pressure and particle velocity, of the shocked material are given by eqs.(2). With this follows

$$\delta = \frac{Z_T * Z_P^2}{(Z_T + Z_P)^2} * \frac{v_P^2}{c_L}. \quad (8)$$

In Table 8 some more data of the experiments, masses  $m_p$  and diameters  $D_p$  of the projectiles, are reported. The three last columns contain calculated results, the kinetic energy of the projectile,  $E_p$ , the compression of the

material in the wave,  $\epsilon$ , (eq.(7)), the initial pressure  $\sigma_A$  (eq.(2)), and the specific wave energy in the target,  $\delta$ , (eq.(8)). The diameter  $D_p$  is put into brackets for the pointed projectiles since it was not directly related to the impact event.

With the reported experiments only the initial phase in the order of 10 microseconds of the total loading and fracturing event is investigated. It is, therefore, assumed that the kinetic energy of the projectiles,  $E_p$ , is not of importance in most cases because of the projectile length being too large for waves travelling back and forth in that short time. This quantity is listed, though, in Table 8 for completeness and shows instructively how it varies throughout the experiments. However, there is no direct correlation to the results.

Instructive is also the calculated compression  $\epsilon$  within the wave. For the pointed impacts the given numbers are valid only at the contact site.

The initial pressure  $\sigma_A$  of the wave generated with the impact and in the plane impact experiments maintained for a few microseconds may be of importance for the production of cracks, since with a reflexion at boundaries tensile forces of the same absolute value can occur which then may exceed the strength threshold.

The last column shows the specific energy of the wave field. This quantity is given in terms of  $\text{MJ/m}^3$  ( $\equiv \text{J/cm}^3$ ) and is used in the diagram of Figs.60 and 61.

It must be taken into account that in those experiments with the projectile being a pointed one (these six experiments are represented by the upper block in Table 8)

the quantities  $\varepsilon$ ,  $\sigma_A$ , and  $\xi$  are not constant in time because of the geometric divergence of the wave. Also with the plane impact the validity of the situation sketched by eqs. (2) and (6) to (8) is limited to a few microseconds only. Finally, this theory is valid only for an elastic halfspace which means all data are of limited accuracy. The diameters  $D_P$  of the pointed projectile are not directly involved in the impact event and, therefore, put into parenthesis.

#	$v_P$ m/s	$m_P$ kg	$D_P$ mm	$E_P$ kJ	$\varepsilon$ $\cdot 10^{-3}$	$\sigma_A$ GPa	$\xi$ MJ/m <sup>3</sup>
998	162	0.133	(50)	1.75	8.2	3.4	28
997	239	0.135	(50)	3.86	12.1	5.1	61
5556	519	0.050	(20)	6.73	26.3	11.0	289
5567	687	0.050	(20)	11.80	34.8	14.5	507
5554	774	0.050	(20)	14.98	39.3	16.4	643
5558	1210	0.050	(20)	36.60	61.4	25.6	1572
1000	101	0.258	49	1.32	5.1	2.1	11
996	194	0.277	49	4.27	9.8	4.1	40
5570	707	0.050	20	12.50	35.9	15.0	537
5542	1062	0.013	12.7	7.33	53.9	22.5	1211

Table 8 State and energy evaluation

In Fig.60 the crack velocity data (Table 6) are plotted versus the energy density data of Table 8. These data points suggest straight lines fitting two regimes in each of the two data casts (pointed and plane impact). These regimes may be explained as follows (see also Fig.59, with the numbers of cracks plotted versus the impact velocity):

At the very beginning a steep increase indicates that all wave energy may be used by a few (1 to  $\approx 4$ ), originally generated cracks only in order to gain speed. However, there also exist limits which correspond to the fracture mechanics terminal crack velocity. In contrary to what was observed with glass experiments, these limits are not very distinct and there are two, depending on the energy density of the wave field. They begin with about 80% of the correlated wave velocity indicated by a knee in the curve. Wave velocities seem to be the ultimate limits, the Rayleigh wave velocity for pointed impacts and the longitudinal wave velocity for plane impacts. This is in contradiction to fracture mechanics results where experience shows that the crack speed never can approach a wave velocity.

The energy consumption mechanism is assumed to change with the knee of the two curves. Instead of augmenting the crack speed significantly with increasing energy the number of cracks seems to increase (see Fig.59). This is demonstrated with the plane impact experiments. Only shots # 1000 and # 996 have countable numbers of cracks, the two others show what is called "field". The situation is shifted somewhat with the pointed impacts. These all show countable numbers of cracks, but still their number seems to increase with impact velocity, although a crack field cannot not be found in any of these experiments.

Nucleation processes responsible for the high "damage velocities" with the glass experiments [3] were also observed in some cases with the ceramic targets. However, a contribution to the observed high crack velocities cannot

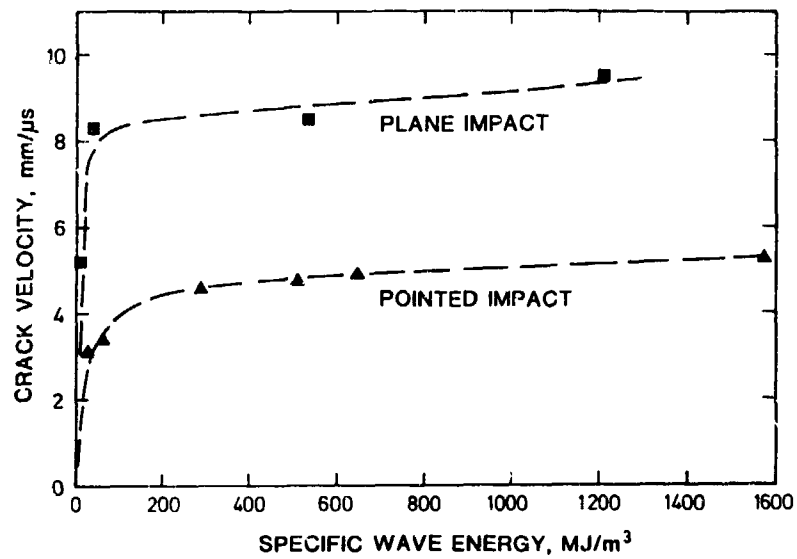


Fig.60 Crack velocity vs. energy density of the wave

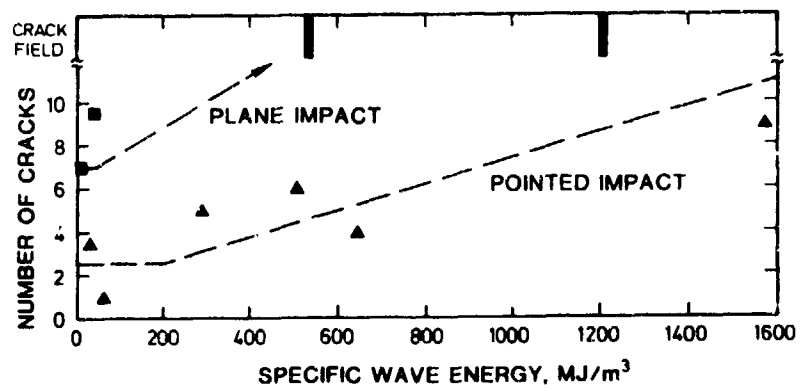


Fig.61 Number of cracks vs. energy density of the wave

be stated. The nucleation mechanism seems to be different from the one in the glass tiles. An example is shot # 1000 (Fig.40). Within only one microsecond (picture # 13 to 14) an entire crack field appears. This is not unlike the spallation process with a certain threshold being exceeded instantaneously in a large field. Compared again with the glass observations, a large number of crack nuclei, all exhibiting the same nucleation threshold, seems to be activated at the same time, probably in a homogeneous stress field, whereas the measured crack velocities seem to be simple crack extension velocities, not influenced by these nucleation effects.

#### 7.2.2 Influence of impact area

Figs.60 and 61 suggest that mainly two mechanisms separated by the knee of the curve are responsible for the fracture process. They also suggest that the product of the two curves,  $v_c(\delta)$  and the corresponding  $C(\delta)$  could result in a straight line. This combination of the number of cracks with the crack speed  $v_c$  delivers the rate of generated crack area:

$$\dot{A} = \frac{C * d * a}{t} = C * d * v_c, \quad (9)$$

with sample thickness  $d = 9.5\text{mm}$  and time  $t$  necessary to produce  $C$  cracks of the length  $a$ .  $A$  is the total crack area. This procedure is sketched in Fig.62. The suggestion is, therefore, that the rate of crack area is proportional to the available energy:

$$\dot{A} = m * \delta. \quad (10)$$

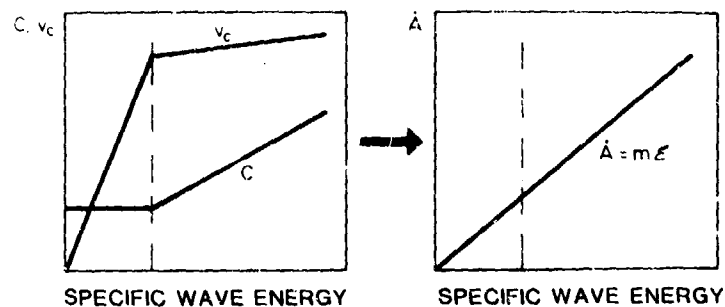


Fig.6.2 Schematic diagrams of equivalent functions

This is documented in Table 9 for all experiments together with the input data, for the rate of fracture area from eq.(9) and for the slope  $m$  from eq.(10). In those cases where a range of crack numbers is given in Tables 4 and 5 two values have been calculated, one for the lower and one for the upper range value. The accuracy of the determined rate of crack area is rather poor because of the difficulty to tell a valid crack number  $C$ . Consequently, the calculated slope  $m$  is also unaccurate. However, tendencies can be observed with the slope in comparison with the impact area. The mean value of all pointed impact experiments differs considerably from the one with a blunt projectile, and even these blunt experiments show different values. In order to also involve those experiments where only a crack field could be seen an estimation was made on the number of cracks from the pictures. All these calculated slopes are listed in Table 10. The result of # 998 has not been included into the pointed mean value since this one is almost one order of magnitude larger than all the other ones for an unknown reason. The results listed in

#	$v_p$ m/s	$\bar{x}$ MJ/m <sup>3</sup>	C	$v_c$ mm/ $\mu$ s	$\dot{A}$ m <sup>2</sup> /s	m m <sup>4</sup> /MNs
998	162	28	3	3.1	88	3.1
998			4	3.1	118	4.2
997	239	61	1	3.4	32	0.52
5556	519	289	4	4.6	175	0.61
5556			6	4.6	262	0.91
5567	687	507	8	4.7	357	0.70
5554	774	643	6	4.9	279	0.43
5558	1210	1572	9	5.3	453	0.29
1000	101	11	5	5.2	247	22
996	194	40	6	8.3	473	12
996			13	8.3	1025	26
5570	707	537	f (30)	8.5	2423	4.5
5542	1062	1211	f (50)	9.5	4513	3.7

Table 9 Crack evaluation

pointed	(998)	$\bar{m} = 3.7$
pointed		$\bar{m} = 0.55 \pm 0.2$
blunt 49mm		$\bar{m} = 20 \pm 7$
blunt 20mm	(5570)	$m = 4.5$
blunt 12.7mm	(5542)	$m = 3.7$

Table 10 Slopes

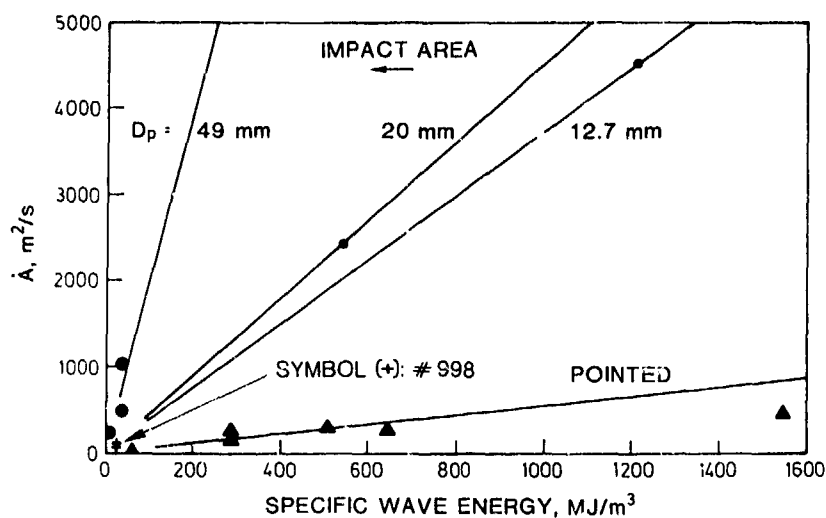


Fig.63 Rate of fracture area vs. available energy

Tables 9 and 10 are illustrated in Fig.63. Although from Fig. 62 it can be expected that the slope of eq.(10) may change with the transition from one energy absorbing mechanism to the other (dashed lines) this cannot be verified by the experiments since their number is not sufficient.

The step from the left to the right diagram in Fig.62 indicated by an arrow is described by eq.(9). The slopes  $m_l$  of the straight lines in Fig.63 (see also Tables 9 and 10) have been calculated by eq.(10).  $m$  is a constant if all factors are constant and the  $\mathcal{E}$  field distribution being homogeneous. If on the other hand  $m$  is found constant also in a divergent  $\mathcal{E}$  field (pointed impact) also  $\dot{A}$ , i.e. the crack velocity  $v_c$  and/or the crack number  $C$ , must decrease.

Within the time span investigated slowing down crack speeds were not observed. In some cases a reduction of the number of cracks could be seen (# 998 for example). However, there are also examples where the number of cracks seems to increase with time (e.g. # 1000). One mechanism of this phenomenon seems to be bifurcation of cracks.

#### 8. DISCUSSION AND CONCLUSIONS

It has been shown that the shadow optical method successfully can be applied to investigate damage phenomena in opaque materials. Considerable efforts had to be undertaken to prepare specimens in a suitable way for these optical purposes. Methods have been developed to grind, lapp, and polish alumina tiles and even those out of harder materials like titanium boride. With the alumina samples it turned out to be necessary to improve the reflectivity of the polished surface by an evaporated aluminum layer. This will not be required with titanium boride and other electric conductive ceramics.

The accuracy of the interrupted light beam trigger could be improved by a new electronic device and for cases where light beams fail a contact trigger was successfully applied.

The very high wave velocities of ceramic materials do not provide much time for the registration of events on the relatively small area of the target. This was experienced drastically with the Cranz-Schardin camera being capable for a  $1\mu\text{s}$  minimum picture separation time only. A factor of

two in the speed of the camera would have doubled the evaluable number of pictures and improved the accuracy of the measured data. At the end of the contract program the puls generator of the camera was rebuilt, therefore, to make the camera faster. It was possible to increase the speed of the camera by a factor of 5. The minimum time distance between two pictures now is  $0.2\mu\text{s}$ .

Even though the reported experiments were run with the "slow"  $1\mu\text{s}$  camera remarkable results could be collected:

Onset and progress of the failure process could be visualized with both, the generation of macroscopic fracture and the damage zone (black area) at the impact site.

Even tiny details of crack formation and propagation could be resolved. For example, it was observed with the low velocity pointed impact experiments that cracks were able to close and disappear again. From this is concluded that plastic deformations must be of a microscopic scale. Another observation is that on most of the high speed pictures cracks look very rough, often like a brush. The roughness seems to indicate that these cracks move with their maximum speed. These rough crack surfaces, however, could not be found anymore on the recovered parts. An example is # 998, Fig.48b, showing the fracturing situation at the  $23^{\text{rd}}$  microsecond including fuzzy cracks. The recovered parts of the sample being put together in Fig.48a do not show this appearance anymore. All these tiny cracks must have closed again, but, nevertheless, must still be there.

To the knowledge of the authors no material is known

which does not exhibit a terminal crack velocity in the range of half the Rayleigh wave velocity. Surprisingly, alumina does not show this in the presented experiments. Without the background of the glass experiments the conclusion would have been drawn that the special loading method applied with this type of experiments causes this strange behaviour and not the material. The glass "was able to help itself" in the same situation by forming what was called "damage velocity" by the nucleation processes and to maintain this way the terminal crack velocity of  $\approx 1500\text{m/s}$  for glasses which has been known since many decades. The investigated ceramic material, however, does not behave like any known material. A physical explanation has not yet been found.

Within the present contract energy absorption could be correlated with macroscopic fracturing only. Two mechanisms mainly could be distinguished, one in the low impact velocity region with an increase in input energy resulting in growing crack speed but not in an augmenting crack number. The other mechanism works in the high impact velocity region showing just the opposite, with almost no increase in the crack velocity but an increasing number of cracks when the input energy grows.

In the upper region of impact velocities, however, the larger amount of energy absorption is assumed to be expended for particle comminution purposes. Future investigations of energy consumption mechanisms will also have to take into account comminution processes.

#### 9. ACKNOWLEDGEMENT

We are thankful for the financial support of this work by the European Research Office of the U.S. Army, London, represented by Dr. W.C. Simmons. Also appreciated is the technical interest and support of Dr. D. Viechnicki, M. Slavin, and G. Quinn, all from AMTL, Watertown, MA. The experiments were performed by J. Gonschorek, D. Preuss, J. Schüier, and E. Zipfel. The ceramographical work was carried out by A. Grussenmeyer, the fractographical work by Miss M. Aberham. We also appreciate valuable discussions which we had with our colleagues, especially with Dr. W. Klemm.

10. REFERENCES

- [1] H.SENF, H.ROTHENHAUSLER, W.PAVEL, H.-J.RAATSCHEN and R.SCHWARZ,  
Analysis of Experimental and Numerical Investigations with Rigid Projectiles Impacting Glass Targets of Differing Physical Quality,  
Journal de Physique, Colloque C3, Supplément au no9, Tome 49, Int.Conf.on Mech. and Phys. Behaviour of Mat. under Dyn.Loading, 1988
- [2] W.PAVEL, H.J.RATSCHEN, R.SCHWARZ, H.SENF, H.ROTHENHAUSLER,  
Experimental and Numerical Investigations of the Failure Behaviour of Glass Targets Under Impact Loading by Rigid Projectiles,  
Proc. 10th Intern. Symp. on Ballistics, San Diego, 1987
- [3] U.HORNEMANN, H.ROTHENHAUSLER, H.SENF, J.F.KALTHOFF, S.WINKLER,  
Experimental Investigation of Wave and Fracture Propagation in Glass Slabs Loaded by Steel Cylinders at High Impact Velocities,  
Inst. Phys. Conf. Ser. No.70, 3rd Conf. Mech. Prop. High Rates of Strain, Oxford 1984
- [4] D.VICHNICKI, W.BLUMENTHAL, M.SLAVIN, C.TRACY, H.SKEELE,  
Armor Ceramics - 1987,  
Proc. Third Tacom Armor Coordinating Conference, Monterey, CA, Febr. 17-19, 1987
- [5] C.TRACY, M.SLAVIN, D.VIECHNICKI,  
Ceramic Fracture During Ballistic Impact,  
Advances in Ceramics, Vol.22, Fractography of Glass and Ceramics, pp.295-306, 1988
- [6] J.E.Field,  
Investigation of the Impact Performance of Various Glass and Ceramic Systems,  
Final Technical Report, US-Army, ERO London, England, Contract Number DAJA45-85-C-0021, August 1988

- [7] J.F.KALTHOFF,  
The Shadow Optical Method of Caustics,  
Chapter 9, Handbook On Experimental Mechanics,  
Society for Experimental Mechanics, Inc.,  
A.S.Kobayashi, Ed., Prentice-Hall, Inc. Englewood  
Cliffs, New Jersey, pp.430-500, 1986
- [8] S.WINKLER,  
Wave and Fracture Phenomena in Impacted Ceramics,  
2nd Periodic Report, Contract No. DAJA45-88-C-0011,  
European Research Office of the U.S. Army, London,  
IWM Report V 15/88
- [9] L.BERGMANN,  
Der Ultraschall und seine Anwendung in Wissenschaft  
und Technik,  
S.Hirzel Verlag, Stuttgart, 1954
- [10] J.S.RINEHART,  
On Fractures Caused by Explosions and Impacts,  
Quarterly of the Colorado School of Mines, Vol.55,  
No.4, Golden, Colorado, October 1960
- [11] E.H.YOFFÉ,  
"The Moving Griffith Crack",  
Phil. Mag. 42, pp.739 to 750, 1951
- [12] K.B.BROBERG,  
"The Propagation of a Brittle Crack",  
Ark.Fiz. 18, pp.159 to 192, 1960
- [13] L.B.FREUND,  
"Crack Propagation in an Elastic Solid Subjected to  
General Loading", I and II,  
J. Mech. Phys. Solids, 20, pp.129 to 152, 1972

## 11. APPENDIX

### Ceramography of the Investigated Material

Material: Alumina, 98%  $\text{Al}_2\text{O}_3$ , as delivered

Type: CeramTec A 18 96, (HOECHST),

Color: white

Size: 100mm \* 100mm \* 10mm

Mass Density  $\rho$ : 3793kg/m<sup>3</sup>

Longitudinal Sound Velocity  $c_L$ : 10 440m/s

Flexural Strength: 0.4 GPa (4-point 40/20mm) 4.5mm \* 3.5mm

Compressive Strength: 4 GPa

Elastic Modulus: 360 GPa

Hardness: 85 HRC 45

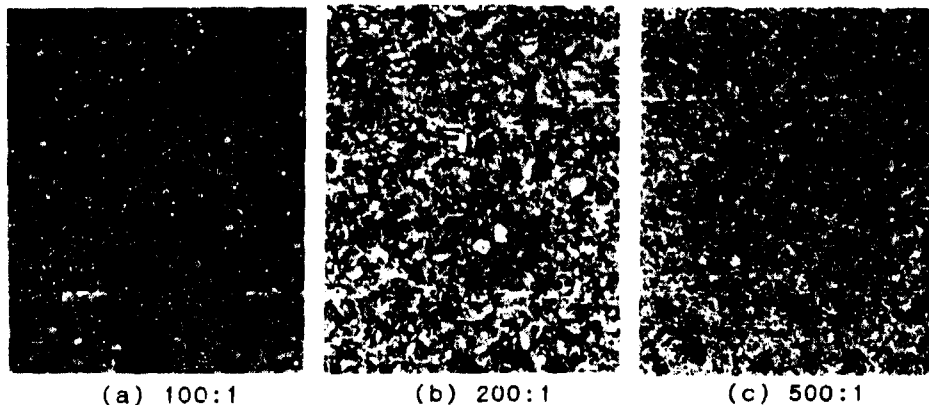


Fig.A1 Micrographs of the material after etching with 85%  $\text{H}_3\text{PO}_4$ , boiling

Grain size: (200 samples)

Length: 1.66  $\mu\text{m}$  (min), 27.25  $\mu\text{m}$  (max), 8.27  $\mu\text{m}$  (mean)

Width: 0.45  $\mu\text{m}$  (min), 17.56  $\mu\text{m}$  (max), 3.62  $\mu\text{m}$  (mean)

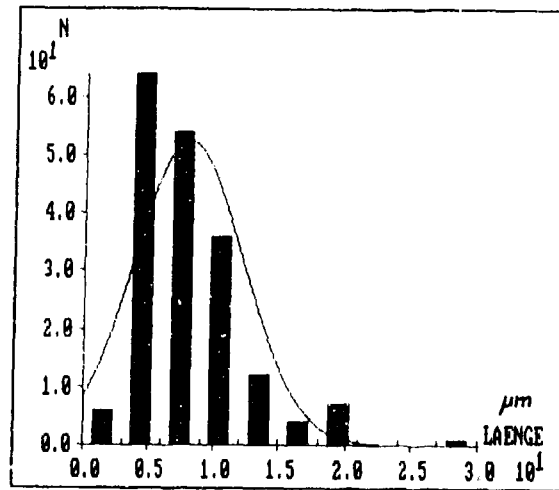


Fig.A2 Distribution of length population vs. length of grains

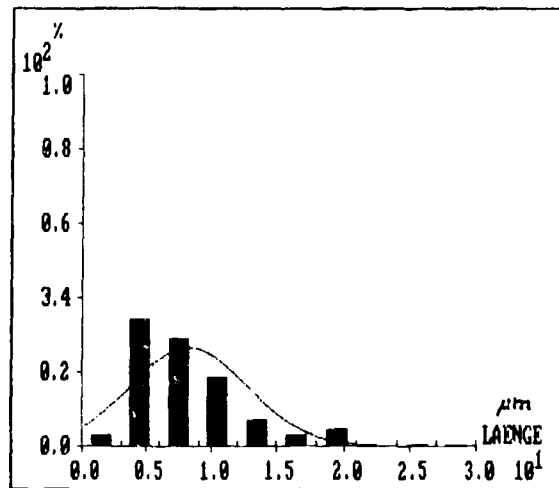


Fig.A3 Percentage of length population vs. length of grains